NOAA Technical Memorandum NWS TDL-57

A PREDICTIVE BOUNDARY LAYER MODEL

Wilson A. Shaffer
Paul E. Long, Jr.

Techniques Development Laboratory
Silver Spring, Md.
May 1975

noaa NATIONAL OCEANIC AND ATMOSPHERIC ADMINISTRATION / National Weather Service

NOAA TECHNICAL MEMORANDA

National Weather Service, Techniques Development Laboratory Series

The primary purpose of the Techniques Development Laboratory of the Office of Systems Development is to translate increases of basic knowledge in meteorology and allied disciplines into improved operating techniques and procedures. To achieve this goal, the laboratory conducts applied research and development aimed at the improvement of diagnostic and prognostic methods for producing weather information. The laboratory performs studies both for the general improvement of prediction methodology used in the National Meteorological Service and for the more effective utilization of weather forecasts by the ultimate user.

NOAA Technical Memoranda in the National Weather Service Techniques Development Laboratory series facilitate rapid distribution of material that may be preliminary in nature and which may be published formally elsewhere at a later date. Publications 1 through 5 are in the former series, Weather Bureau Technical Notes (TN), Techniques Development Laboratory (TDL) Reports; publications 6 through 36 are in the former series, ESSA Technical Memoranda, Weather Bureau Technical Memoranda (WBTM). Beginning with TDL 37, publications are now part of the series NOAA Technical Memoranda, National Weather Service (NWS).

Publications listed below are available from the National Technical Information Service (NTIS), U.S. Department of Commerce, Sills Bldg., 5285 Port Royal Road, Springfield, Va. 22151. Prices vary for paper copy; $1.45 microfiche. Order by accession number, when given, in parentheses at end of each entry.

Weather Bureau Technical Notes

TN 10 TDL 1 Objective Prediction of Daily Surface Temperature. William H. Klein, Curtis W. Crockett, and Carlos R. Dunn, September 1965. (PB-168-590)

TN 11 TDL 2 Hurricane Cindy Galveston Bay Tides. N. A. Pore, A. T. Angelo, and J. G. Taylor, September 1965. (PB-168-608)

TN 29 TDL 3 Atmospheric Effects on Re-Entry Vehicle Dispersions. Karl R. Johannessen, December 1965. (PB-169-381)

TN 45 TDL 4 A Synoptic Climatology of Winter Precipitation From 700-mb. Lows for the Intermountain Areas of the West. Donald L. Jorgensen, William H. Klein, and August F. Korte, May 1966. (PB-170-635)

TN 47 TDL 5 Hemispheric Specification of Sea Level Pressure From Numerical 700-mb. Height Forecasts. William H. Klein and Billy M. Lewis, June 1966. (PB-173-091)

ESSA Technical Memoranda

WBTM TDL 6 A Fortran Program for the Calculation of Hourly Values of Astronomical Tide and Time and Height of High and Low Water. N. A. Pore and R. A. Cummings, January 1967. (PB-174-660)

WBTM TDL 7 Numerical Experiments Leading to the Design of Optimum Global Meteorological Networks. M. A. Alaka and Frank Lewis, February 1967. (PB-174-497)

WBTM TDL 8 An Experiment in the Use of the Balance Equation in the Tropics. M. A. Alaka, D. T. Rubsam, and G. E. Fisher, March 1967. (PB-174-501)

WBTM TDL 9 A Survey of Studies of Aerological Network Requirements. M. A. Alaka, June 1967. (PB-174-984)

WBTM TDL 10 Objective Determination of Sea Level Pressure From Upper Level Heights. William Klein, Frank Lewis, and John Stackpole, May 1967. (PB-179-949)

WBTM TDL 11 Short Range, Subsynoptic Surface Weather Prediction. H. R. Glahn and D. A. Lowry, July 1967. (PB-175-772)

WBTM TDL 12 Charts Giving Station Precipitation in the Plateau States From 700-Mb. Lows During Winter. Donald L. Jorgensen, August F. Korte, and James A. Bunce, Jr., October 1967. (PB-176-742)

WBTM TDL 13 Interim Report on Sea and Swell Forecasting. N. A. Pore and W. S. Richardson, December 1967. (PB-177-038)

WBTM TDL 14 Meteorological Analysis of 1964-65 ICAO Turbulence Data. DeVer Colson, October 1968. (PB-180-268)

WBTM TDL 15 Prediction of Temperature and Dew Point by Three-Dimensional Trajectories. Ronald M. Reap, October 1968. (PB-180-727)

WBTM TDL 16 Objective Visibility Forecasting Techniques Based on Surface and Tower Observations. Donald M. Gales, October 1968. (PB-180-479)

WBTM TDL 17 Second Interim Report on Sea and Swell Forecasting. N. A. Pore and W. S. Richardson, January 1969. (PB-182-273)

WBTM TDL 18 Conditional Probabilities of Precipitation Amounts in the Conterminous United States. Donald L. Jorgensen, William H. Klein, and Charles F. Roberts, March 1969. (PB-183-144)

WBTM TDL 19 An Operationally Oriented Small-Scale 500-Millibar Height Analysis Program. Harry R. Glahn and George W. Hollenbaugh, March 1969. (PB-184-111)

WBTM TDL 20 A Comparison of Two Methods of Reducing Truncation Error. Robert J. Bermowitz, May 1969. (PB-184-741)

WBTM TDL 21 Automatic Decoding of Hourly Weather Reports. George W. Hollenbaugh, Harry R. Glahn, and Dale A. Lowry, July 1969. (PB-185-806)

WBTM TDL 22 An Operationally Oriented Objective Analysis Program. Harry R. Glahn, George W. Hollenbaugh, and Dale A. Lowry, July 1969. (PB-186-129)

WBTM TDL 23 An Operational Subsynoptic Advection Model. Harry R. Glahn, Dale A. Lowry, and George W. Hollenbaugh, July 1969. (PB-186-389)

WBTM TDL 24 A Lake Erie Storm Surge Forecasting Technique. William S. Richardson and N. Arthur Pore, August 1969. (PB-185-778)

(Continued on inside back cover)

NOAA Technical Memorandum NWS TDL-57

A PREDICTIVE BOUNDARY LAYER MODEL

Wilson A. Shaffer
Paul E. Long, Jr.

Techniques Development Laboratory
Silver Spring, Md.
May 1975

UNITED STATES
DEPARTMENT OF COMMERCE
Rogers C. B. Morton, Secretary

NATIONAL OCEANIC AND
ATMOSPHERIC ADMINISTRATION
Robert M. White, Administrator

National Weather
Service
George P. Cressman, Director

CONTENTS

A PREDICTIVE BOUNDARY LAYER MODEL[1]

Wilson A. Shaffer[2] and Paul E. Long, Jr.[3]
Techniques Development Laboratory
National Weather Service, NOAA
Silver Spring, Md. 20910

ABSTRACT. A large scale three-dimensional planetary boundary layer model to predict temperature, humidity, and wind in the atmosphere's lowest 2 km is being developed at the Techniques Development Laboratory of the United States National Weather Service. At present, a one-dimensional model is being run which consists of twelve levels within two layers--a 50-m thick surface layer having constant fluxes of heat, momentum, and moisture, and a transition layer extending upward to 2 km. Surface layer fluxes and eddy diffusion coefficients are calculated following a Monin-Obukhov formulation, using the empirical results of Businger et al. (1971), Dyer (1967), and Webb (1970). The time-dependent wind, humidity, and temperature equations are solved in the transition layer using assumed, but variable, diffusion coefficient profiles. A complete radiation treatment, including atmospheric hearing due to flux divergences, is included.

Surface temperature is calculated through a simple, efficient energy balance. The fluxes of surface layer latent and sensible heat, net radiation, and soil heat are combined in a highly nonlinear energy equation, which is solved iteratively for surface temperature. Soil heat flux is calculated employing a simple analytic solution of the soil heat equation. This solution requires an initial soil temperature profile and assumes that the soil heat coefficients are constant in depth. The solution has the advantage of not requiring computation levels within the soil. Tests using Australian Wangara data (Clarke et al., 1971) and O'Neill data (Lettau and Davidson, 1957) for initialization show good agreement between predicted and measured boundary layer winds and temperatures.

---

[1] Presented at the Symposium on the Atmospheric Boundary Layer, Oct. 10-12, 1973, Mainz, Germany.

[2] National Research Council Postdoctoral Associate

[3] Research performed principally while a National Research Council Postdoctoral Associate

I. INTRODUCTION

At the Techniques Development Laboratory of the U.S. National Weather Service, we are building an atmospheric boundary layer model for prediction of low-level temperature, humidity, and wind. The planned three-dimensional model will operate on the 25 x 25 grid labelled BLM in figure 1. The model's grid spacing will be approximately 80 km in the horizontal. For comparison, the hemispheric Primitive-Equation model (PE) and the Limited-Area Fine Mesh model (LFM) are shown with their respective grid mesh sizes. The National Meteorological Center's Planetary Boundary Layer model (PBL) is an adaptation of the U.S. Air Force's model described in Hadeen and Friend (1972). This model is run on the LFM grid of approximately 160 km and uses Ekman-type winds.

II. PRESENT ONE-DIMENSIONAL MODEL

The model we are developing is presently run (experimentally) in one dimension (figure 2). The model extends from the surface to 2 km and has two distinct layers--a transition layer in which the time-dependent equations for temperature, humidity, and wind are solved and a 50-m thick contact (or surface) layer in which the Businger-Webb contact layer relationships are assumed. The transition layer has 12 vertical grid levels, spaced logarithmically using the coordinate transformation

$$Z' = Z'(Z) = A \ln \left[1 + \frac{Z-h}{A}\right] + h \quad ; A \gg h; \ \Delta Z' = 50\text{m. (const.)}$$

Upper boundary conditions for the model will be supplied from a free air model (either the PE or the LFM) for T, q, and wind. At the surface, an energy balance is used to calculate surface temperature and humidity.

Within the transition layer the time-dependent equations for potential temperature, θ; humidity, q; and wind are solved:

$$\frac{\partial \theta}{\partial t} + \vec{V} \cdot \nabla \theta = \frac{\partial}{\partial z} \left(K_T \frac{\partial \theta}{\partial z}\right) + \text{Radiative heating}$$

$$\frac{\partial q}{\partial t} + \vec{V} \cdot \nabla q = \frac{\partial}{\partial z} \left(K_q \frac{\partial q}{\partial z}\right)$$

$$\frac{\partial u}{\partial t} + \vec{V} \cdot \nabla u = \frac{\partial}{\partial z} \left(K_m \frac{\partial u}{\partial z}\right) + f\,(v - v_g)$$

$$\frac{\partial v}{\partial t} + \vec{V} \cdot \nabla v = \frac{\partial}{\partial z} \left(K_m \frac{\partial v}{\partial z}\right) + f\,(u_g - u).$$

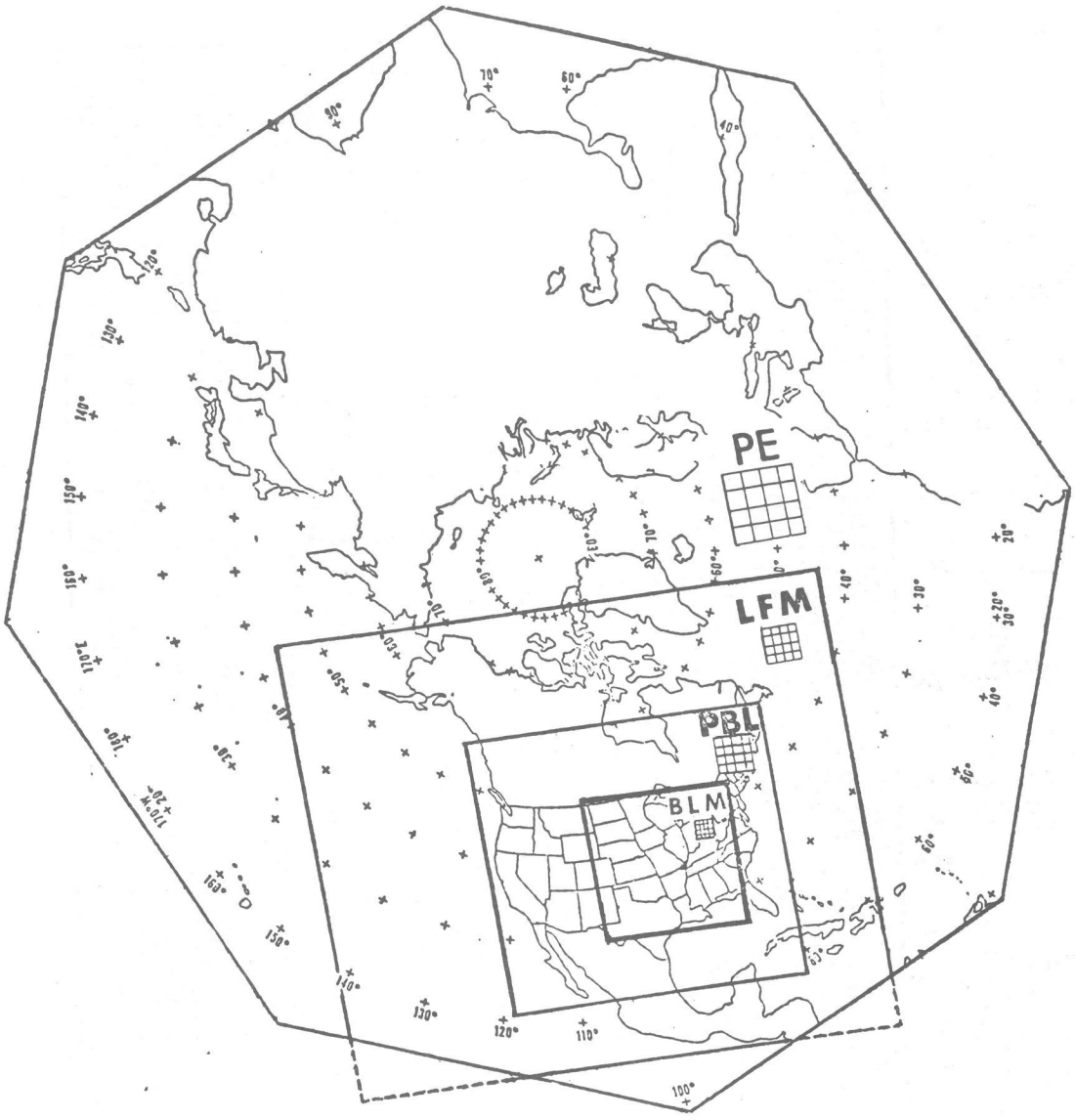

Figure 1.--Relative sizes of the TDL Boundary Layer Model (BLM), Primitive-Equation Model (PE), Limited Area Fine Mesh Model (LFM), and the Planetary Boundary Layer Model (PBL).

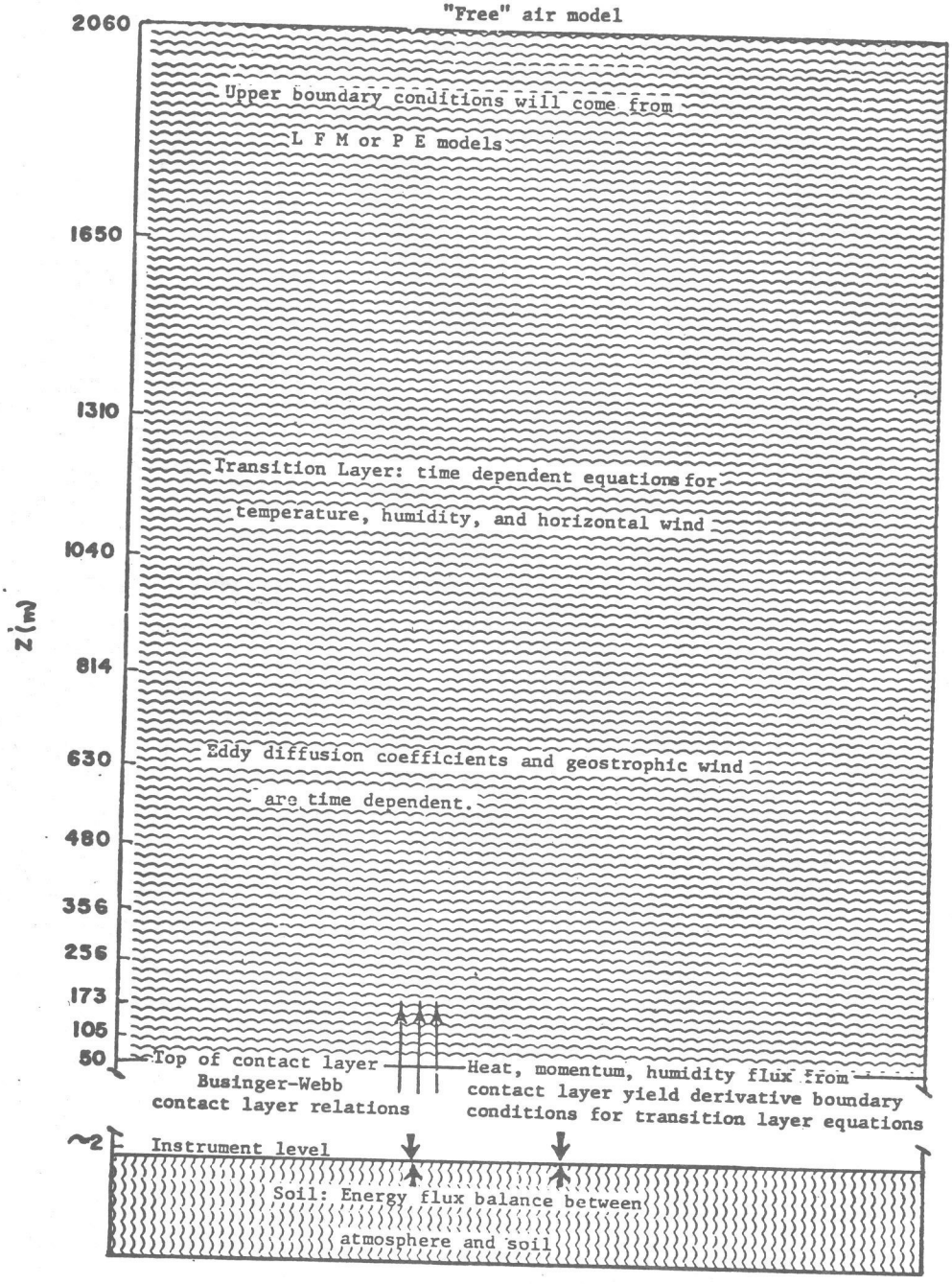

Figure 2.--Physical structure of the present one-dimensional model.

Table 1.--List of Major Symbols

A	parameter for vertical coordinate transformations
c_p	specific heat capacity of air at constant pressure
c_j	fraction of cloud cover in layer j
C_i	fraction of clouds in the i^{th} category
C_{ij}	fraction of clear sky between levels i and j
E	latent heat flux; in the surface energy balance, emissivity matrix for longwave radiation
$\mathcal{E}$	net energy flux at the surface
f	Coriolis parameter
$f_o(Z)$	initial soil temperature profile
F	soil heat flux; radiation flux
g	gravitational acceleration
g_j	coordinate transformation term, $\frac{dZ'}{dZ}$
$g(x,t)$	forcing function used in the non-linear, advection-like equation
$\tilde{G}$	complex geostrophic variable, $U_g + iV_g$
H	assumed top of the constant-flux layer
H	top of the boundary layer model; ratio of actual latent heat flux to potential latent heat flux
i	$\sqrt{-1}$; in radiation calculations, short wave radiation intensity
k	von Karman's constant; in soil heat flux calculations, soil thermal diffusivity
K	eddy diffusion coefficient; in soil heat flux calculations, soil thermal conductivity
L	Obukhov length
$\mathcal{L}$	latent heat of evaporation
p	pressure
q	specific humidity
q_*	friction humidity
R_{net}	net long wave and short wave radiation flux at the surface
S	bulk stability parameter

Table 1.--Continued

t	time
T	temperature; cloud transmission coefficient
$\tilde{T}$	complex temperature-humidity: $\Theta + iq$
u	east-west wind component; in radiation calculations, optical path length between layers
u_g	east-west geostrophic wind component
u_*	friction velocity
U	horizontal wind speed
v	north-south wind component
v_g	north-south geostrophic wind component
$\vec{V}$	wind vector
W	optical path length
$\tilde{W}$	complex horizontal wind, $u + iv$
Z	vertical coordinate; solar zenith angle
Z'	transformed vertical coordinate
Z_i	height of instrument level
Z_o	surface roughness length
Z_{soil}	vertical soil coordinate, positive downward
Δ	difference operators; Δu - difference in U between the surface and h; $\Delta\Theta$ - difference in Θ between the surface and h; Δt, Δx - finite differences increments in time and space
∇	gradient operator
δ_m, δ_r	momentum and temperature constants in the Businger profile relationships for the constant - flux layer
ε	long wave emissivity
ζ	dummy variable used in soil heat integrals
Θ	potential temperature
Θ_*	friction temperature
$\bar{\Theta}$	average potential temperature
ρ	density
σ	Stefan-Boltzmann constant

Table 1. Continued

τ	transmitted short wave radiation in the absence of water vapor
ϕ_t, ϕ_m, ϕ_q	Monin-Obukhov universal functions for temperature, momentum, and humidity

In each case, the $\vec{V}\cdot\nabla(\ )$ term is assumed to be zero for the one-dimensional model. These four equations reduce to two by introducing new complex variables $\tilde{T} = \Theta + iq$ and $\tilde{W} = u + iv$:

$$\frac{\partial \tilde{T}}{\partial t} + \vec{V}\cdot\nabla\tilde{T} = \frac{\partial}{\partial z}\left(K_T \frac{\partial \tilde{T}}{\partial z}\right)$$

$$\frac{\partial \tilde{W}}{\partial t} + \vec{V}\cdot\nabla\tilde{W} = \frac{\partial}{\partial z}\left(K_m \frac{\partial \tilde{W}}{\partial z}\right) - if\,(\tilde{W} - \tilde{G})$$

where a new complex geostrophic wind is defined as

$$\tilde{G} = u_g + i\,v_g$$

and K_q is assumed to equal K_T.

These complex equations are advanced forward in time using a Crank-Nicolson finite-difference scheme, shown here for temperature ($W, \nabla\Theta = 0$):

$$\frac{\Theta_j^{n+1} - \Theta_j^n}{\Delta t} = g_j \Big\{ g_{j-1/2} K_{j-1/2}^n \Theta_{j+1}^{n+1} - (g_{j-1/2} K_{j-1/2}^n + g_{j+1/2} K_{j+1/2}^n)\,\Theta_j^{n+1}$$

$$- g_{j+1/2} K_{j+1/2}^n \Theta_{j+1}^{n+1} + g_{j-1/2} K_{j-1/2}^n \Theta_{j-1}^n$$

$$- (g_{j-1/2} K_{j-1/2}^n + g_{j+1/2} K_{j+1/2}^n)\,\Theta_j^n$$

$$+ g_{j+1/2} K_{j+1/2}^n \Theta_{j+1}^n \Big\} \Big/ 2(\Delta Z')^2.$$

$$g(Z) = \frac{dZ'}{dZ}.$$

A Monin-Obukhov similarity formulation is used to determine profiles of wind, temperature, and humidity within the contact (or surface) layer:

$$\frac{\partial \Theta}{\partial Z} = \frac{\Theta_*}{kZ}\,\phi_T\left(\frac{Z}{L}\right) \qquad L = \frac{u_*^2\,\overline{\Theta}}{kg\Theta_*}$$

$$\frac{\partial q}{\partial Z} = \frac{q_*}{kZ}\,\phi_q\left(\frac{Z}{L}\right)$$

$$\frac{\partial U}{\partial Z} = \frac{u_*}{kZ}\,\phi_m\left(\frac{Z}{L}\right).$$

The non-dimensional functions, ϕ, are taken from the empirical relations of Businger et al. (1971). Also, the functions ϕ_T and ϕ_q, for temperature and moisture, respectively, are assumed to be equal. Von Karman's constant, k, is given as 0.35.

For the unstable case, the functions of Businger et al. are

$$\phi_T = \phi_q = .74 \quad (1 - \gamma_T \frac{Z}{L})^{-1/2} \qquad \phi_m = (1 - \gamma_m \frac{Z}{L})^{-1/4}$$

and for the mildly stable case, they become

$$\phi_T = \phi_q = .74 + 4.7 \frac{Z}{L}$$

$$\phi_m = 1. + 4.7 \frac{Z}{L}$$

where $\gamma_T = 9$ and $\gamma_m = 15$.

In order to obtain u_*, Θ_*, q_*, and L from values of $\Delta\Theta$, ΔU, and Δq, the Businger relationships are first integrated:

$$\Delta\Theta \equiv \int_{Z_i}^{h} \frac{\partial\Theta}{\partial Z} dZ = \frac{u_*}{K} [\quad]_\Theta$$

$$\Delta U \equiv \int_{Z_o}^{h} \frac{\partial U}{\partial Z} dZ = \frac{u_*}{k} [\quad]_u$$

h = top of surface layer
Z_i = instrument level
Z_o = roughness length

$$L = \frac{u_*^2 \bar{\Theta}}{kg\Theta_*}$$

For the unstable case, the bracketed quantities are

$$[\quad]_\Theta = 0.74 \ln \left\{ \frac{\left(\sqrt{1 - \gamma_T \frac{h}{L}} - 1\right)\left(\sqrt{1 - \gamma_T \frac{Z_i}{L}} + 1\right)}{\left(\sqrt{1 - \gamma_T \frac{h}{L}} + 1\right)\left(\sqrt{1 - \gamma_T \frac{Z_i}{L}} - 1\right)} \right\}$$

and

$$[\quad]_u = \ln \left\{ \frac{\left[\left(1 - \gamma_m \frac{h}{L}\right)^{1/4} - 1\right]\left[1 + \left(1 - \gamma_m \frac{Z_o}{L}\right)^{1/4}\right]}{\left[1 + \left(1 - \gamma_m \frac{h}{L}\right)^{1/4}\right]\left[\left(1 - \gamma_m \frac{Z_o}{L}\right)^{1/4} - 1\right]} \right\}$$

$$+ 2\left[\tan^{-1}\left(1 - \gamma_m \frac{h}{L}\right)^{1/4} - \tan^{-1}\left(1 - \gamma_m \frac{Z_o}{L}\right)^{1/4}\right]$$

For the mildly stable case, these quantities become

$$[\quad]_\Theta = 0.74 \ln h/Z_i + 4.7/L \quad (h - Z_i)$$

$$[\quad]_u = \ln h/Z_o + 4.7/L \; (h - Z_o)$$

Rather than iterate over Θ_*, U_*, and L to obtain a solution to these equations, a single parameter

$$S \equiv \frac{\Delta U^2 \bar{\Theta}}{g \Delta \Theta}$$

is formed. The integrated profile relations may be written,

$$L = \frac{[\quad]_\Theta}{[\quad]_u^2} \; S.$$

In the unstable case, the value must be iterated over L.

In the stable case, L is a root of a quadratic equation:

$$a L^2 + bL + c = 0$$

where $a = \ln^2 h/Z_o$; $b = 9.4 \; (h - Z_o) \ln \frac{h}{Z_o} - 0.74 \; S \ln \frac{h}{Z_i}$;

$c = [4.7 \; (h - Z_o)]^2 - 4.7 \; S \; (h - Z_i)$.

For very stable cases, the root may be complex or less than h. In either case, a Webb profile is used above L to the top of the contact layer,

$$\left.\begin{aligned} \phi_T &= 0.74 + 4.7 = 5.44 \\ \phi_m &= 1. + 4.7 = 5.7 \end{aligned}\right\} \quad Z > L$$

giving

$$[\quad]_\Theta = 0.74 \ln L/Z_i + 4.7 (L - Z_i)/L + 5.44 \ln(h/L)$$

$$[\quad]_u = \ln L/Z_o + 4.7 (L - Z_o)/L + 5.7 \ln(h/L).$$

As with the unstable case, the strongly stable case requires iteration. Adequate convergence usually occurs in three steps.

With L known, u_*, Θ_*, q_*, $K_T(h)$, $K'_T(h)$, $K_m(h)$ $K'_m(h)$

$$\left.\frac{\partial \Theta}{\partial Z}\right)_h, \quad \left.\frac{\partial U}{\partial Z}\right)_h, \text{ and } \quad \left.\frac{\partial q}{\partial Z}\right)_h,$$

are easily computed.

The system of equations for the model is closed by specifying the diffusion coefficients throughout the transition layer. (Although closure through a turbulent energy equation appears more desirable from a physical standpoint, the lack of consensus on closure schemes and the additional computer time which they require was considered a drawback for an operational model at this time.) An O'Brien (1970) cubic interpolation for K(z) is used. K is assumed to be small and K' is set equal to zero at the top of the boundary layer model. The K and K' values at the bottom of the transition layer are those calculated at the top of the contact layer. Thus, the K profile varies in time with changes in the contact layer. The O'Brien K profile always has its maximum at H/3, fixed for a fixed depth of the boundary layer model. We have run some experiments in which H is proportional to u_*,

$$H = cu_*.$$

This has the effect of lowering the boundary layer at night and increasing it during the day.

A flow diagram of the boundary layer model's computations is given in figure 3.

III. SURFACE ENERGY BALANCE

As mentioned earlier, an energy flux balance at the surface is used to calculate the surface temperature and humidity. Sensible and latent heat fluxes are calculated using their usual contact layer definitions:

$$F_{\substack{\text{Sensible}\\ \text{Heat}}} = -\rho c_p u_* \Theta_* \; ; \; F_{\substack{\text{Latent}\\ \text{Heat}}} = -\rho \mathcal{L} u_* q_*$$

where c_p is the specific heat (at constant pressure) of air and $\mathcal{L}$ is the latent heat of evaporation. Since q_* is related to Θ_* in the model through the relationship

$$q_* = \Theta_* \left(\frac{q_h - q_{sfc}}{\Theta_h - \Theta_{sfc}}\right),$$

an assumption to determine the surface humidity must be made. At present, the ratio of actual evaporation to potential evaporation is held constant throughout the day (Halstead et al. 1957)

SOLUTION OF THE PROGNOSTIC EQUATIONS

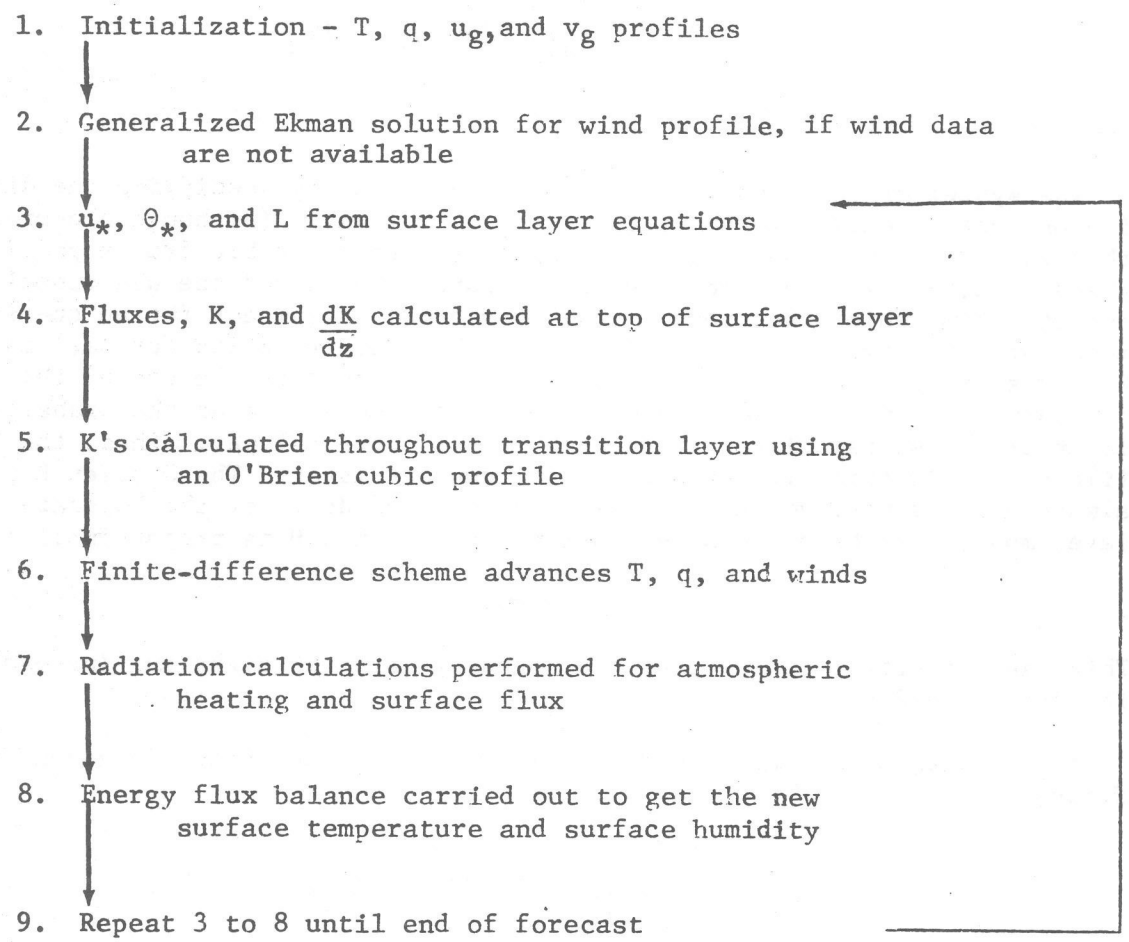

Figure 3.--General outline of calculations in the one-dimensional boundary layer model.

$$H = \frac{E_{actual}}{E_{potential}} = \frac{q_h - q_{sfc}}{q_h - q_{sfc\ (saturated)}}.$$

This allows the surface humidity to be calculated readily.

The incident long and short wave radiation fluxes (discussed later) are calculated and combined into a radiation term, R_{net}, which excludes the flux emitted at the surface. As will be demonstrated, the soil heat flux reduces to a linear expression in surface temperature when an analytic solution is used. Combining each of these fluxes gives the energy flux equation:

$$\mathcal{E} = 0 = \rho c_p u_* \theta_* + \rho L u_* q_* - (C\ T_{sfc} + C') - \varepsilon_s\ \sigma T_{sfc}^4 + R_{net}$$

where C and C' are constants depending upon soil thermal coefficients and previous soil heat fluxes (see section IV), and where ε_s is the surface's long wave emissivity.

Since u_*, θ_*, and q_* depend upon the surface temperature and surface emission varies as T^4, the energy equation is highly non-linear. A Newton-Raphson iteration technique is used to solve for temperatures:

$$T_{new} = T_{old} - \frac{\mathcal{E}(T_{old})}{\left(\frac{\partial \mathcal{E}}{\partial T}\right)_{T_{old}}}.$$

Although each iteration requires a new contact layer calculation of u_* and θ_*, the scheme is quite efficient. In general, only 2 or 3 iterations are required for convergence, which is assumed when

$$|T_{new} - T_{old}| \leq 0.05^{\circ}C.$$

IV. SOIL HEAT FLUX

An analytic solution of the heat equation is used to calculate soil heat flux. Two basic assumptions are made: 1) the soil thermal coefficients do not vary with depth and 2) the initial soil temperature profile is known. In order to solve the heat equation, two boundary conditions are necessary. At the air-soil interface, a heat flux F(t) enters the soil. The second condition is that the soil temperature approaches a constant value as the depth is increased. Measurements show that soil temperature varies little below 1 or 2 meters over a 24-hour period, justifying the use of this assumption.

Use of these assumptions in the heat equation gives the temperature at depth Z (positive downward) at time t as

$$T_{soil}(Z, t) = \frac{1}{2\sqrt{\pi\, k\, t}} \int_0^\infty f_o(\zeta) \left\{ e^{-(Z-\zeta)^2/(4kt)} + e^{-(Z+\zeta)^2/(4kt)} \right\} d\zeta$$

$$+ \frac{1}{K} \sqrt{\frac{k}{\pi}} \int_0^t e^{-Z^2/(4\,k\,u)} \frac{F(t-u)}{\sqrt{u}}\, du$$

where $f_o(z)$ is the initial soil temperature profile, F(t) is the surface soil heat flux, K is the thermal conductivity k is the thermal diffusivity and u is a dummy variable. (See Carslaw and Jeager (1959) for example, for a derivation of the above equation.) Only the surface temperature is of interest; at the surface the temperature reduces to

$$T_{sfc}(t) = \frac{1}{\sqrt{\pi\, k\, t}} \int_0^\infty f_o(\zeta)\, e^{-\zeta^2/4\,kt}\, d\zeta$$

$$+ \frac{1}{K} \sqrt{\frac{k}{\pi}} \int_0^t \frac{F(t-u)}{\sqrt{u}}\, du \quad .$$

The first term on the right-hand side is due to redistribution of heat associated with the initial soil temperature profile. The profile is simply integrated with a Gaussian. Solutions for this term using several useful, simple profiles are given in Table 2.

The second term of the soil heat flux equation above is caused by fluxes occuring after t=0. In order to evaluate this term, the flux during each model time step, Δt, is assumed to be linear in time. (Note: The term can also be evaluated by assuming that the soil heat flux is constant during each step. Only a slight change in the final coefficients results.) At time $t = n\Delta t$, the flux that occurred between time $i\Delta t$ and $(i+1)\,\Delta t$ can be written as

$$F = F_{n-i} - \left(\frac{F_{n-i} - F_{n-i-1}}{\Delta t} \right) (u - i\Delta t).$$

Integration during each interval, then summing yields the second term:

$$\frac{4}{3}\sqrt{\frac{k\Delta t}{\pi K^2}} \left\{ F_n + \sum_{i=1}^{n-1} \left[(i+1)^{3/2} + (i-1)^{3/2} - 2i^{3/2} \right] F_{n-i} + \left[(n-1)^{3/2} - n^{3/2} + \frac{3}{2}\sqrt{n} \right] F_0 \right\}.$$

As an example, if a constant initial temperature profile with the initial flux, F_0, equal to zero, is assumed, the surface temperature can be written as

$$T_{sfc}(t = n\Delta t) = T_\infty + \frac{4}{3}\sqrt{\frac{k\Delta t}{\pi K^2}} \left[F_n + \sum_{i=1}^{n-1} C_i F_{n-i} \right].$$

Table 2.-- Evaluation of the soil heat term due to various initial profiles.

Initial Soil Heat Profile	$\frac{1}{\sqrt{\pi kt}} \int_o^\infty f_o(\zeta)\ e^{-\zeta^2/4\ kt}\ d\zeta$
$f_o = T_\infty$ (constant)	T_∞
$f_o = Ae^{-BZ_{soil}}$ (exponential)	$Ae^{B^2kt}\ \text{erfc}\ (B\sqrt{kt}\ )$
$f_o = Ae^{-BZ^2_{soil}}$ (Gaussian)	$A\ (1 + 4\ Bkt)^{-1/2}$

Inverting the equation for the soil heat flux, the flux is linear in the surface temperature

$$F_n = \frac{3}{4}\sqrt{\frac{\pi K^2}{k\Delta t}}\ (T_{sfc} - T_\infty) - \sum_{i=1}^{n-1} C_i F_{n-i} = C\ T_{sfc} + C'.$$

This form is readily adapted to the energy balance and the Newton-Raphson scheme used to solve for surface temperature.

V. LONG WAVE RADIATION FLUX

Long wave radiation and atmospheric heating due to its flux divergence are calculated for each time step of the model. Account is taken of cloud cover in the model and both water vapor and carbon dioxide are considered as emitters of long wave radiation. For water vapor, an increment of optical path length in a layer, dW_{H_2O}, which has density ρ and specific humidity q, is given by

$$dW_{H_2O} = \rho q\ dp.$$

Once these increments of optical path length are obtained, they are summed from the top of the boundary layer to the i^{th} level to give the path length, W_i

$$W_{H_2O}(i) = \sum_{j=1}^{\text{Top of B.L.}} dW_{H_2O}.$$

The emissivity function for water vapor being used was derived by Kuhn (1963) using atmospheric temperature, humidity and long wave radiation measurements. These emissivities, as given in Pandolfo et al. (1971), are

$$E_{i,j} = \begin{cases} 0.1129 \log_{10}(1 + 12.63u) & \text{for} \quad \log_{10} u \le -4 \\ 0.104 \log_{10} u + 0.440 & \log_{10} u \le -3 \\ 0.121 \log_{10} u + 0.491 & \log_{10} u \le -1.5 \\ 0.146 \log_{10} u + 0.527 & \log_{10} u \le -1 \\ 0.161 \log_{10} u + 0.520 & \log_{10} u \le 0 \\ 0.136 \log_{10} u + 0.542 & \log_{10} u > 0 \end{cases}$$

where $u = |W_i - W_j|$ is the optical path length between the i^{th} and j^{th} levels.

In addition to the emission of long wave radiation by water vapor, carbon dioxide emission is considered. Basically the 15-cm band is the only band of significance for CO_2, so emissivities and path length are based on it. No interaction effects between CO_2 and H_2O vapor are considered here (Atwater 1970). Pandolfo's path lengths are used for CO_2

$$dW_{CO_2} = 0.4148\ (p_i - p_{i+1})\ \text{cm/atmos.}$$

which assume a constant CO_2 concentration throughout the atmosphere.

Kondrat'yev's (1969) emissivity function for CO_2 is used:

$$E_{CO_2}(i,j) = 0.185\left[1 - \exp\left(-.3919\left|W_{CO_2}(i) - W_{CO_2}(j)\right|^{0.4}\right)\right].$$

A. Downward Long Wave Flux

The downward flux of long wave radiation at a reference level, j_r, is the sum of the emissions for each layer above, modified by absorption between the layer and j_r, plus the amount of radiation reaching j_r from above the boundary layer. The flux reaching the top of the boundary layer is now assumed to be σT^4_{ABOVE}. (This flux will be calculated in the 3-dimensional model using temperatures and humidities from the large-scale model that supplied dynamic boundary conditions for the model.) Clouds, except cirrus, may be present in any layer and are assumed to radiate as black bodies. Cirrus radiate as "half-black" bodies.

With these assumptions, the downward flux at a level j_r can be expressed as (see figure 4)

$$F_{jr} = \sum_{j=jr}^{top-1}\left[\frac{\sigma}{2}\left(T^4_{j+1} + T^4_{j}\right)\left(E(j_r, j+1) - E(j_r, j)\right) C_{jr,\,j} + \sigma T_j^4\,(1 - E(j_r, j))\, c_j\, C_{jr,\,j+1}\right] + \sigma T^4_{ABOVE}\left[(1 - E(j_r, Top)\right] C_{j_r,\,Top\ of\ B.L.}$$

where $C_{i,j}$ = fraction of clear sky between levels i and j and c_j= fraction of clouds in layer j.

B. Upward Long Wave Flux

The upward flux at any level consists of the amount of reflected long wave flux that is transmitted to the level, plus the amount of radiation emitted below which reaches the level. If ε_S is the surface emissivity (it is not necessary to have a "black" surface), the reflected flux at the surface is

$$F_{refl} = F_{sfc}(1-\varepsilon_S).$$

The upward flux at level j_r can be expressed as

$$F_{jr} = \sum_{j=2}^{jr}\left[\frac{\sigma}{2}\left(T^4_{j-1} + T^4_{j}\right)\left(E(j_r, j-1) - E(j_r, j)\right) C_{jr,\,j-1} + \sigma T_j^4\,(1 - E(j_r, j))\, c_j\, C_{jr,\,j}\right] + (\varepsilon_S\,\sigma\,T^4_{sfc} + F_{refl})\,[1 - E(j_r, sfc)]\, C_{jr,\,sfc}.$$

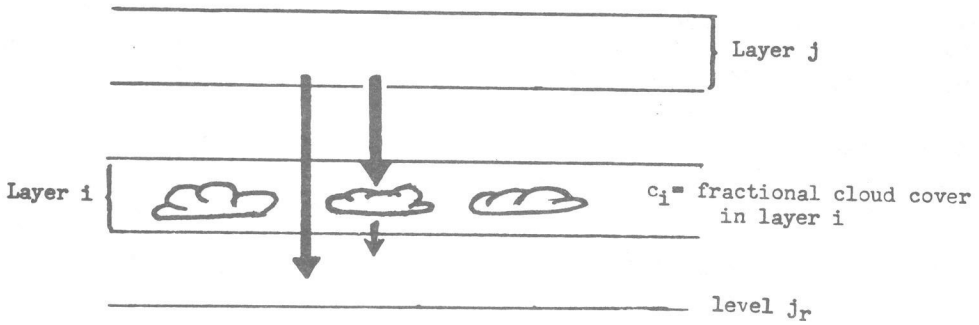

The amount of downward flux reaching j_r from layer j is

$$\sigma T_j^4 \Delta E_j (1-c_i)$$

The amount of flux reaching j_r from layer i is

$$\sigma T_i^4 \Delta E_i (1-c_i) + \sigma T_{\substack{\text{cloud} \\ \text{base}}}^4 c_i (1-E(\text{cloud base}, j_r))$$

Figure 4.--Treatment of long wave radiation, including clouds within the boundary layer.

VI. SHORT WAVE RADIATION FLUXES

Incident on the top of the atmosphere is the solar flux, S_o, of roughly 2.0 cal/cm^2/min. Part of this flux is absorbed due to water vapor and other absorbers in the atmosphere and part is scattered back to space. An expression from McDonald (1960) gives the absorption due to water vapor as

$$A_w = 0.077 \ (U_{Above} \sec Z)^{0.3}$$

where U_{Above} is the optical path length of water vapor above the boundary layer and Z is the solar zenith angle. Transmitted short wave radiation in the absence of water vapor is calculated using Kondrat'yev's expression

$$\tau = 1.041 - 0.16 \left[(0.949 \frac{P_{Top\ of\ B.L}}{P_{surface}} + 0.051) \sec Z \right]^{1/2}$$

which accounts for scattering. The short wave radiation to reach the top of the boundary layer is

$$S_{BL} = \begin{cases} S_o \cos Z \ (\tau - A_w) \ ; & \cos Z > 0 \\ 0 & \text{otherwise} \end{cases}.$$

Clouds appearing above the boundary layer are broken into three categories—high, middle, and low. The fractional covering of each will be estimated from large-scale model humidities. Clouds within the boundary layer make up a fourth class and will eventually be predicted using boundary layer model predicted humidities. Each cloud category has a transmission function (Pandolfo et al. 1971) associated with it:

$$T_{Boundary\ Layer} = 0.25\text{-}0.01 \sec Z$$

$$T_{Low} = 0.35\text{-}0.015 \sec Z$$

$$T_{Middle} = 0.45\text{-}0.01 \sec Z$$

$$T_{High} = 0.9\text{-}0.04 \sec Z$$

where T is the fraction tramsmitted. When clouds are included in the model above the boundary layer, the short wave flux at the boundary layer top becomes

$$S_{BL} = S_{BL} \ (\text{No clouds}) \ \prod_{i=1}^{3} [1 - C_i \ (1 - T_i)]$$

where C_i is the fractional covering in the i^{th} category (figure 5).

Within the boundary layer, Pandolfo's expressions for absorption by water vapor and for scattering are used:

$$di_{H_2O} = - 7.55 \times 10^{-4} \ (u \sec Z)^{- 0.7} \ du$$

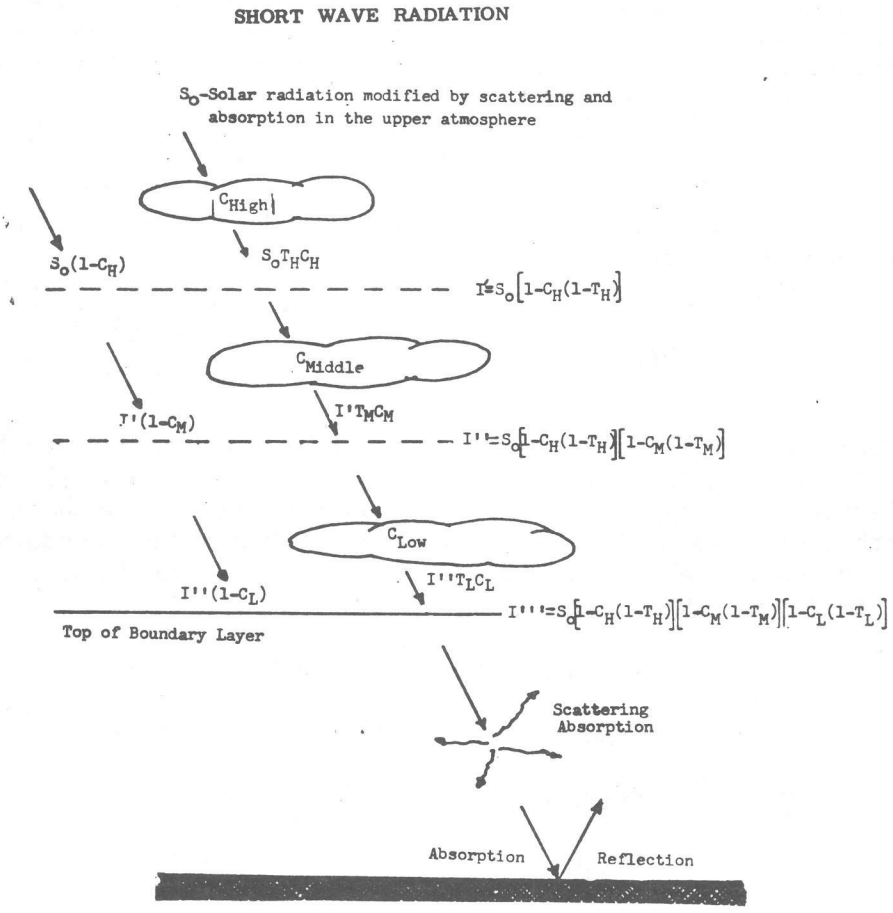

Figure 5.--Treatment of solar radiation.

$$di_{scatt} = -\,2\,S_o\,(3.796 \times 10^{-5})\left[(0.949\,\frac{p_i}{p_o} + 0.051)\sec Z\right]^{-1/2}(p_i - p_{i-1}).$$

The short wave radiation which finally reaches the surface is

$$I_{Surface} = \left[S_{BL}(\text{With clouds}) + \sum_{j=1}^{\text{Top of B.L}} (di_{H_2O} + di_{scatt})_j\right] \times (1 - c_{BL}\,(1 - T_{BL}))$$

where c_{BL} is the fraction of cloud cover within the boundary layer. The amount of radiation absorbed at the surface is

$$I \underset{\text{surface}}{\text{ abs. at }} = (1 - \text{albedo})\, I_{surface}.$$

No account is made of reflected short wave radiation or its heating.

VII. FINITE-DIFFERENCE SCHEMES

An operational model needs an efficient, accurate finite-difference scheme for integrating forward in time. In a study done by Paul Long (1975), several finite-difference schemes used in current boundary layer models were compared using a one-hour time step (figure 6). Needless to say, we're using the Crank-Nicolson scheme! This scheme, used in the transition layer and coupled with the contact layer and the surface, has good stability for time steps as large as 1/2 hour. The finite-difference scheme is stable for much longer time steps. However, holding surface fluxes constant for too long a time step causes unphysical oscillations in the model at sunrise.

Details of these schemes and of the use of chapeau functions and splines in finite-difference schemes (as suggested by Dr. James Bradley at Drexel University) are given in "Some Physical and Numerical Aspects of Boundary Layer Modeling at the Techniques Development Laboratory" by Long and Shaffer (1975). The paper was presented by Paul E. Long at the AMS Conference on Numerical Prediction, in Monterey, Calif.

Two of the most interesting and significant results from that paper are shown in figures 7 to 9. In figures 7 and 8, a finite differencing scheme and a chapeau basis function technique are used to advect a Gaussian-shaped object. A chapeau function has the shape of a hat--its value is 1 at the grid point, and drops linearly to zero at adjacent points. Beyond, the chapeau function is zero (figure 10)

$$f_c = \begin{cases} (X_i - X)/(X_i - X_{i-1}); & X_{i-1} \le X \le X_i \\ (X - X_i)/(X_{i+1} - X_i); & X_i \le X \le X_{i+1} \end{cases}.$$

With this scheme we get fourth-order accuracy.

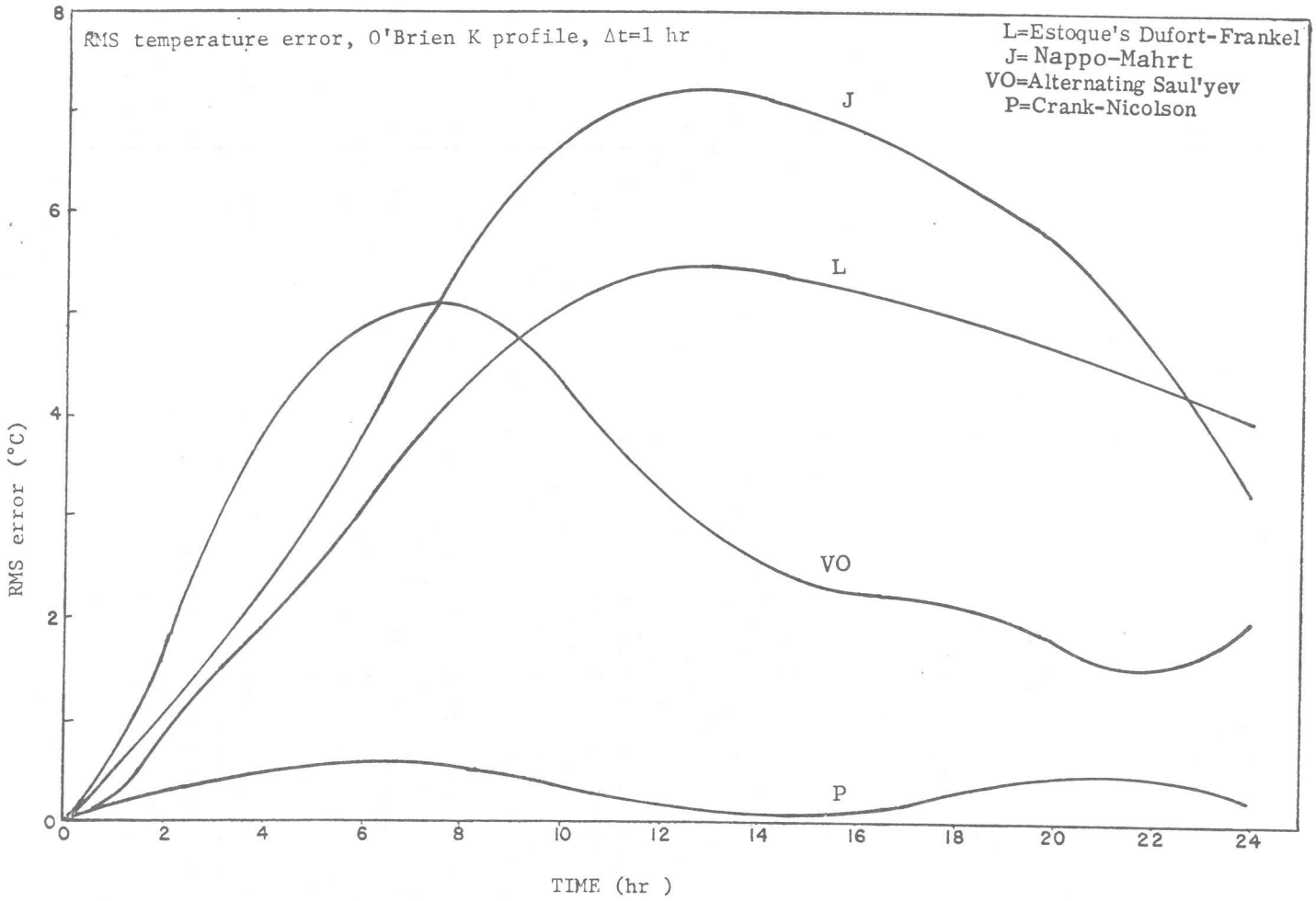

Figure 6.--Four finite-difference schemes used in boundary layer modeling are compared.

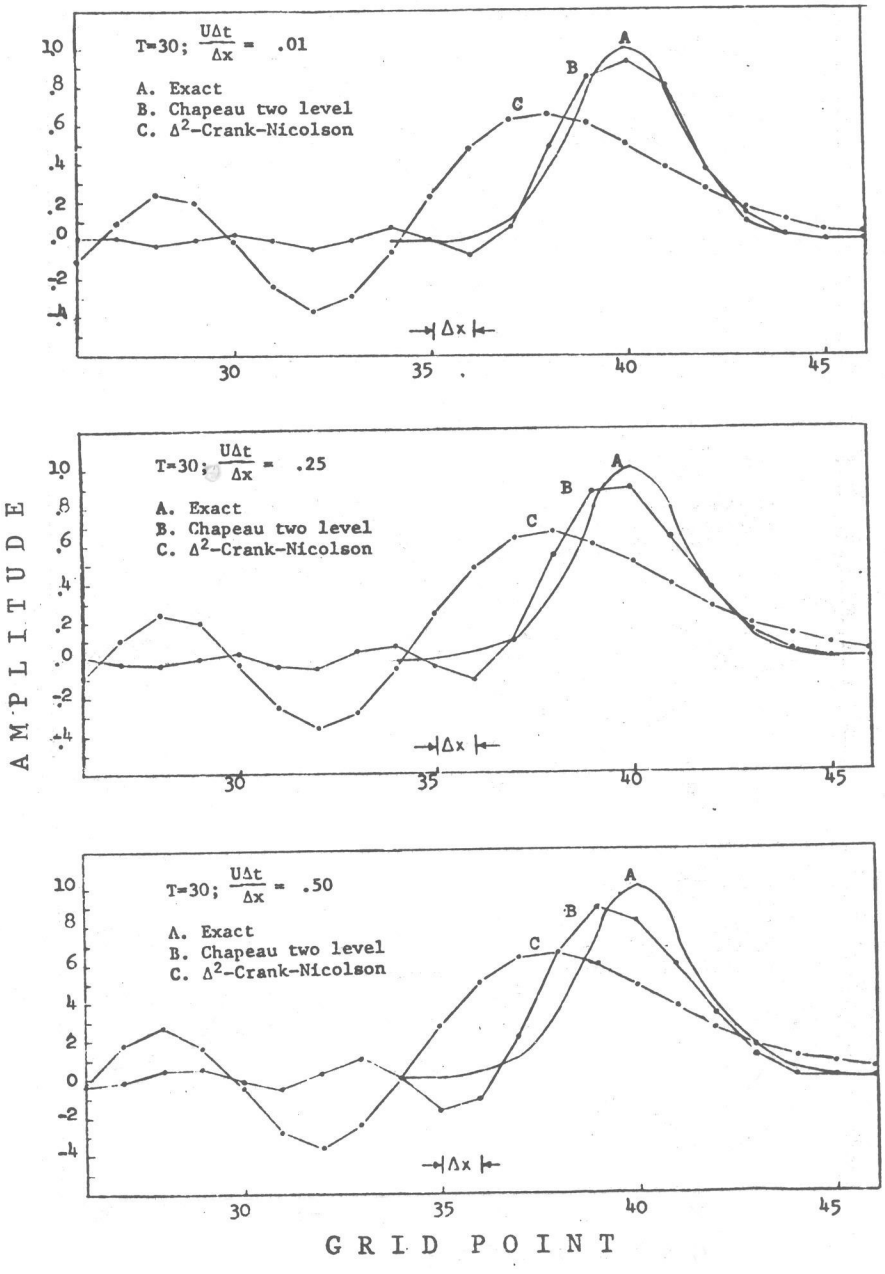

Figure 7.--Comparison of a 2-level chapeau function scheme with a second-order Crank-Nicolson scheme for $U\frac{\Delta t}{\Delta x}$ = .01, .25, and .50.

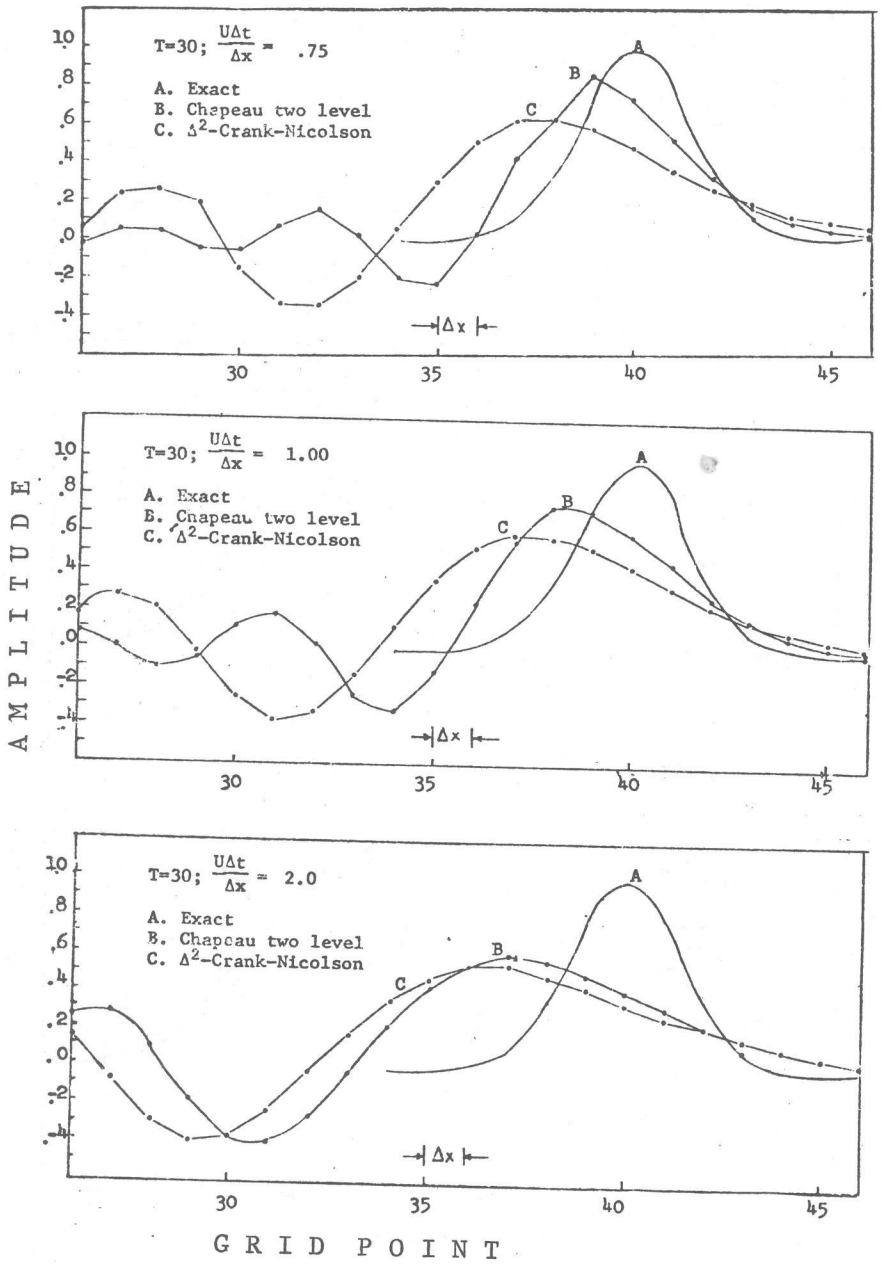

Figure 8.--Comparison of a 2-level chapeau function scheme with a second-order Crank-Nicolson scheme for $\frac{U\Delta t}{\Delta x}$ = 0.75, 1.0, and 2.0.

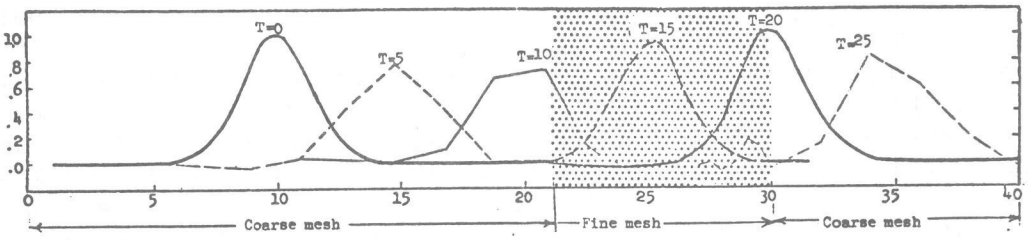

Figure 9.--Evolution of a Gaussian solution of $\frac{\partial u}{\partial t} + u\frac{\partial u}{\partial x} = g(x,t)$ as the Gaussian passes from a coarse mesh region into a fine mesh region, then back out through the coarse region. The ratio of mesh sizes is $\frac{\Delta x(\text{coarse})}{\Delta x(\text{fine})} = 4$.

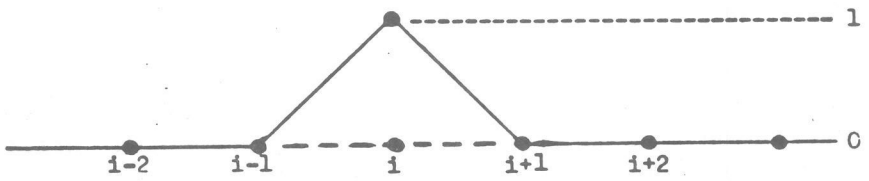

Figure 10.--Form of the chapeau basis function.

Figure 9 shows the same Gaussian advected into a one-dimensional telescoping grid. The ratio of fine mesh to coarse mesh spacing is 1/4. Here, cubic splines are used to obtain the necessary derivatives for the finite-difference scheme. In the coarse grid region, the object decays rapidly. However, as it enters the fine mesh region, the object rebuilds, almost perfectly duplicating the original object. (This is not as amazing as it first appears. A forcing function, g(x,t), is necessary to make the Gaussian a solution to the non-linear advection-like equation. It is this forcing that causes the regeneration.) As the object flows out into another coarse region, deterioration occurs again. Also, a small amplitude reflection propagates back into the fine mesh region. Probably a gradual transition in grid lengths between the coarse and fine mesh regions would diminish the problem.

VIII. TESTS OF THE ONE-DIMENSIONAL MODEL

In order to test the one-dimensional model, simulations of two days of data from the Australian Wangara experiment (Clarke, et al. 1971) and one period of the O'Neill experiment (Lettau and Davidson 1957) were made. The model was initialized using temperature, humidities and wind profiles taken directly from measurements. Soil temperature profiles and thermal coefficients were taken from measurements in the case of the O'Neill data. For the Wangara data, they were prescribed after testing a range of values. In each case, measured values of temperature, humidity, and wind at 2 km were used for upper boundary conditions on the model. Measured cloud cover was used in the model to modify incident radiation. Geostrophic winds were assumed to be time varying, but constant throughout the boundary layer. The O'Neill simulation used measured geostrophic winds. However, since Wangara's observed geostrophic winds proved unreliable, the 2-km wind was substituted for the geostrophic winds.

Simulation of Wangara Day 39 (Aug. 22) of the Australian experiment are shown in figures 11 to 16; Wangara Day 32 in figures 17 and 18; and the O'Neill 5th period in figure 19. In general, predicted surface temperature and energy fluxes show good agreement with their corresponding measurements. Surface winds, although not as accurate, show reasonable agreement. The inaccuracy in wind may be due to the use of 2-km winds as geostrophic winds (in the case of the Wangara simulations) and the assumption that the geostrophic wind is independent of height.

Time cross-sections and plots at various levels for temperature and wind (figures 13 to 16) indicate best agreement near the surface. As height is increased, advection, not accounted for in the model, probably plays an increasingly important role. For example, measured temperatures in the 1 to 1.4-km layer oscillate dramatically during Day 39. Also, the wind cross-section for the same day shows a disturbance propagating downward, beginning about 6 AM at 2 km and reaching the surface about 6 PM.

The importance of including radiative heating of the atmosphere was demonstrated in several tests with the model. Figures 20 and 21 compare two runs using Wangara Day 39 data--one with radiational heating, one without.

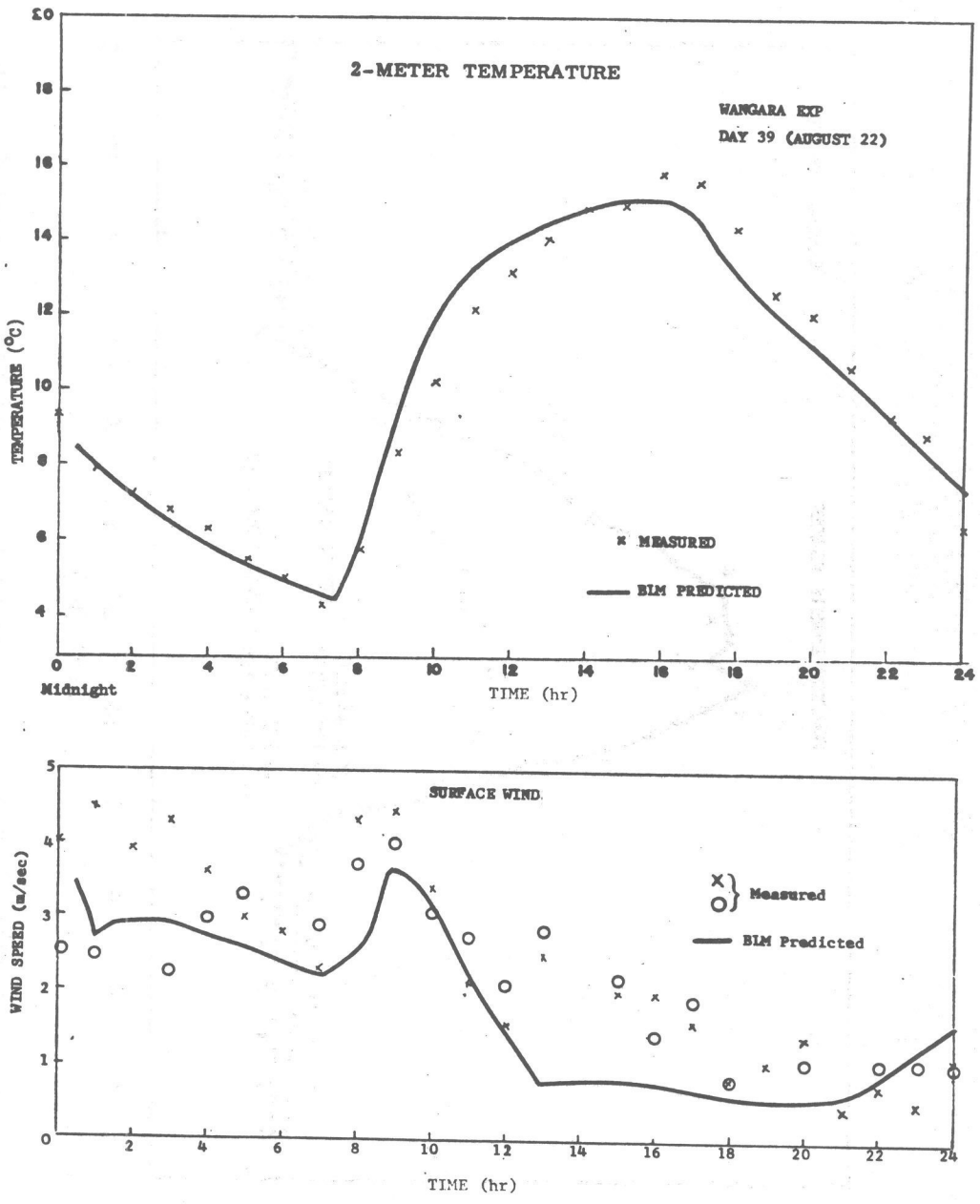

Figure 11.--BLM-simulated surface (2 m) temperatures and (3 m) winds are compared to measured values at the Wangara site, Aug. 22.

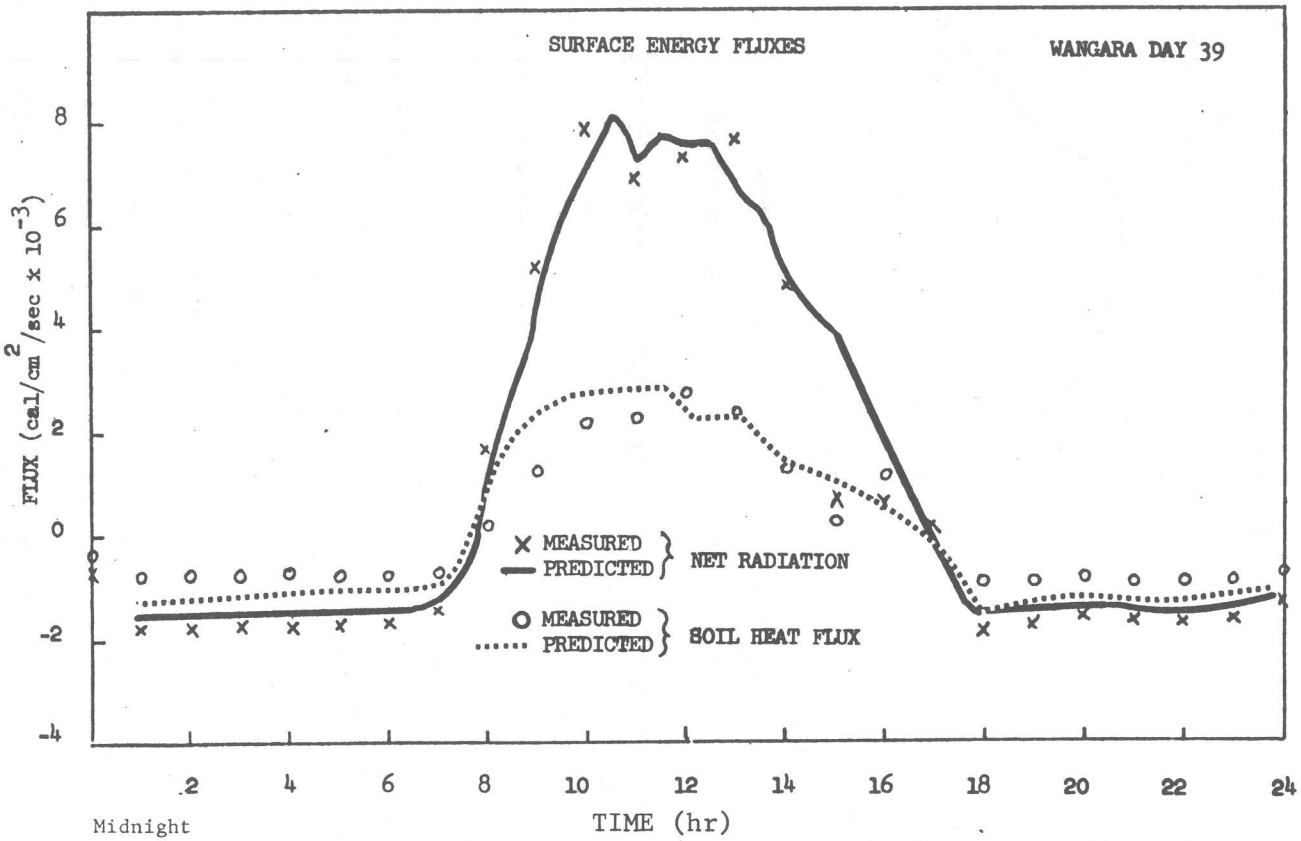

Figure 12.--Surface fluxes of net radiation and soil heat calculated in the BLM simulation are compared to measurements at Wangara, Aug. 22.

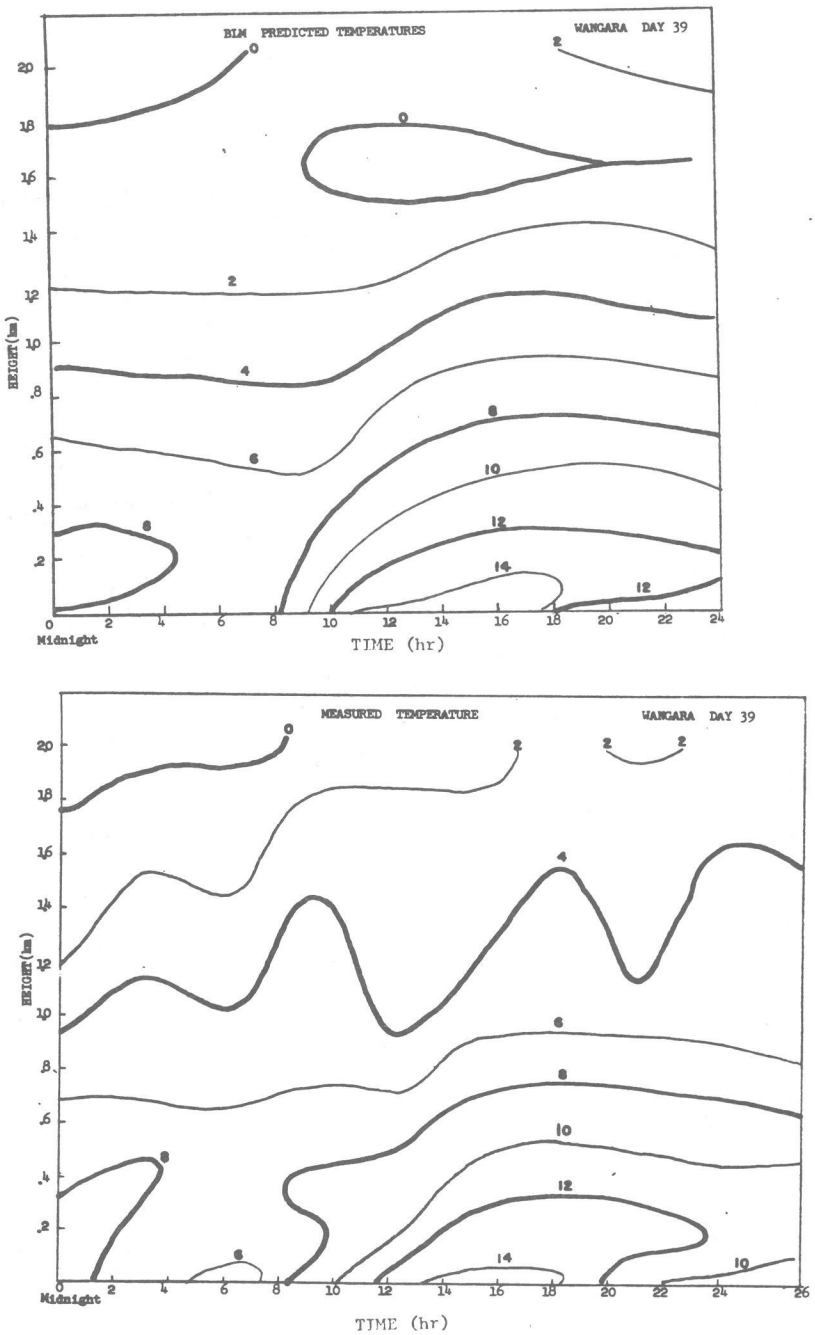

Figure 13.--BLM-predicted temperatures (upper figure) and measured temperatures (lower figure) for Wangara, Aug. 22.

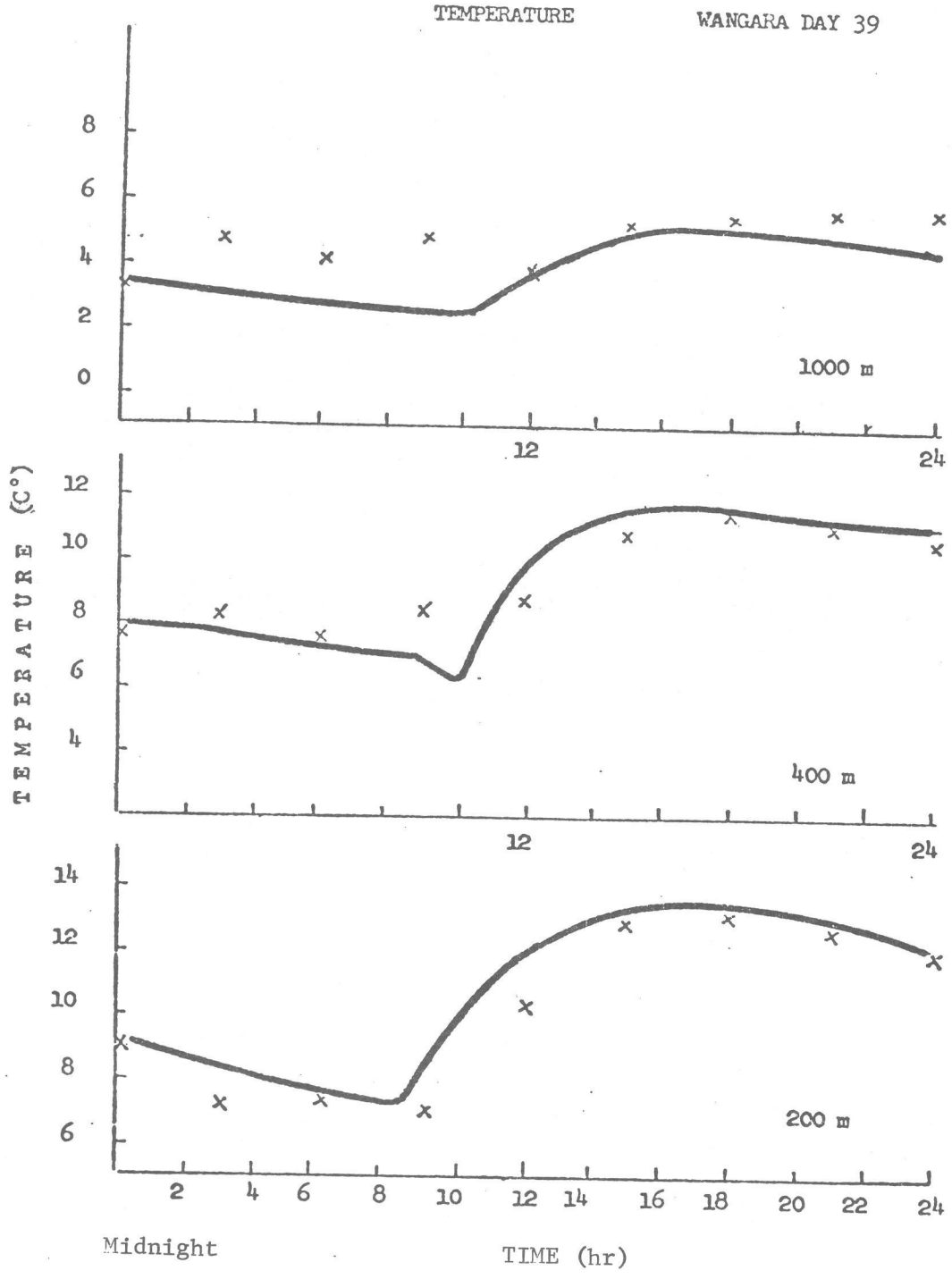

Figure 14.--BLM-simulated temperatures (solid line) and measure temperatures (crosses) are compared at 1000 m, 400 m, and 200 m for Wangara, Aug. 22.

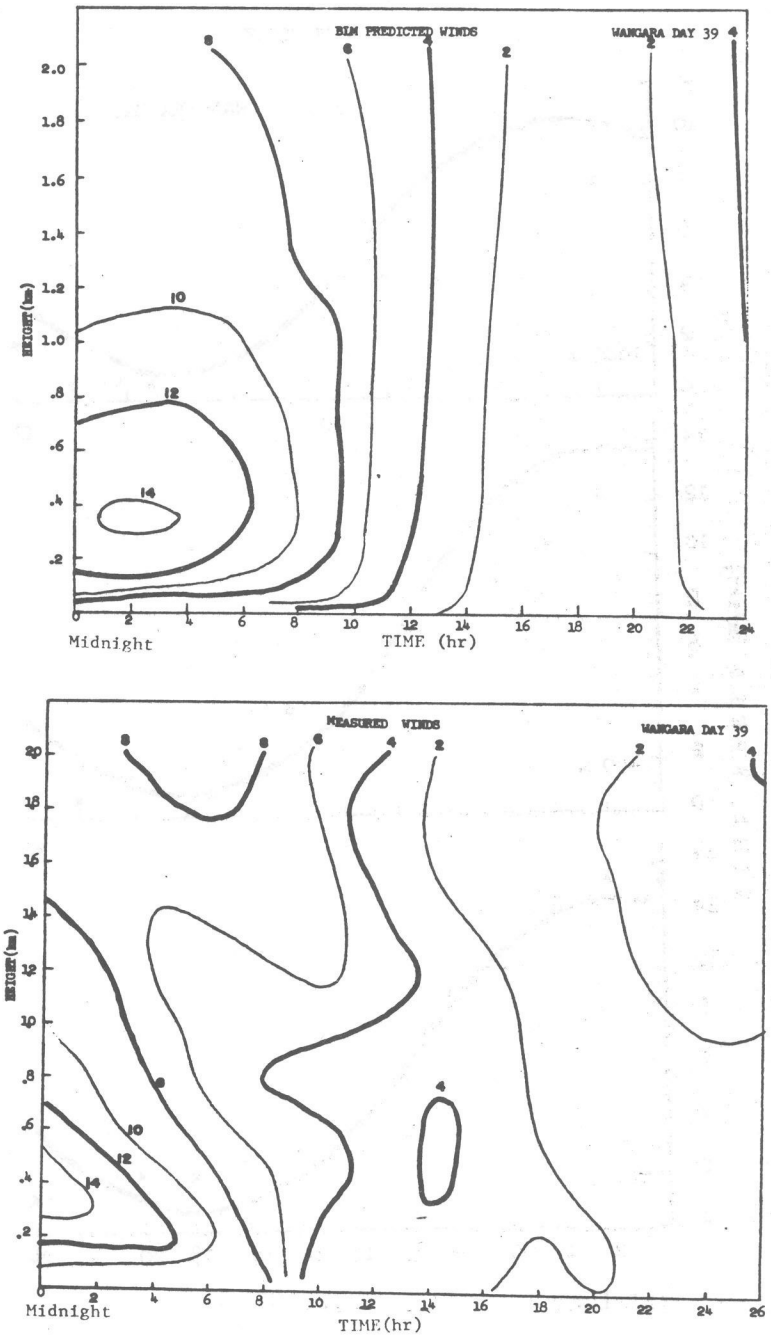

Figure 15.--Wind-time cross-sections for BLM prediction (upper figure) and measured wind (lower figure) are shown.

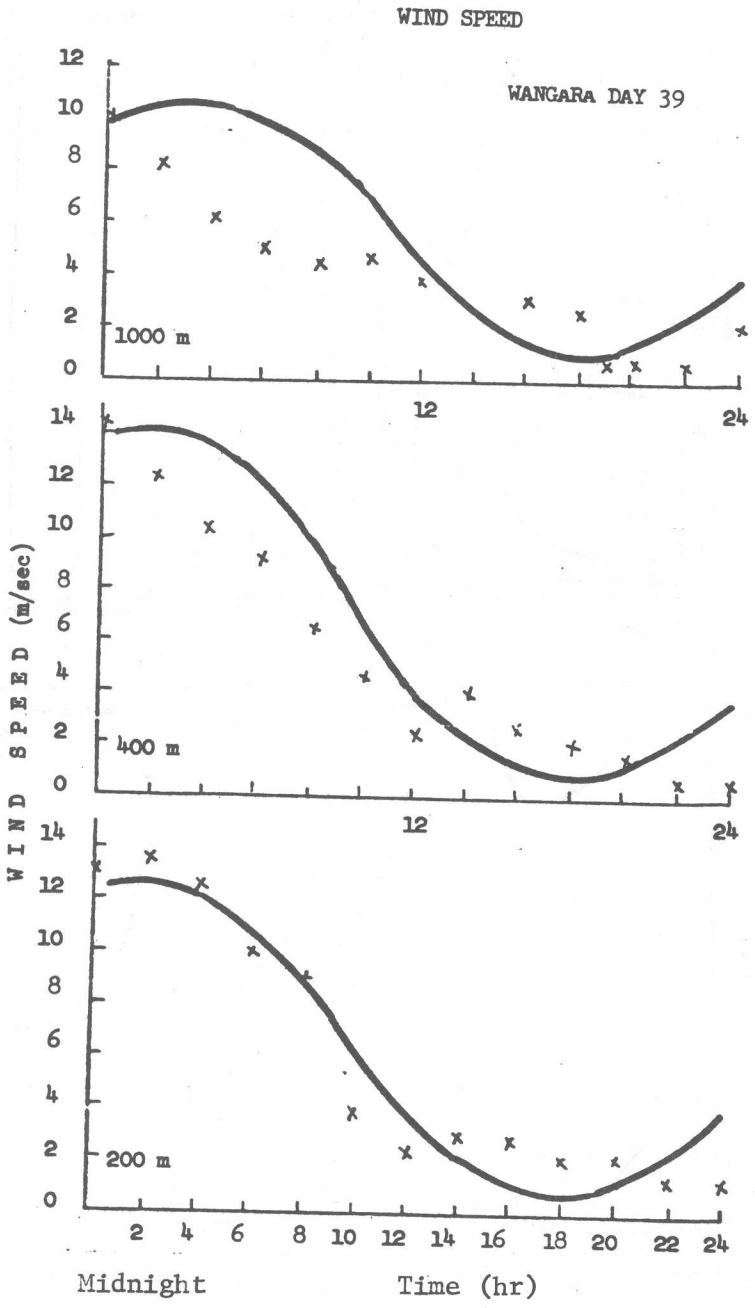

Figure 16.--Winds at 1000 m, 400 m, and 200 m are shown for Wangara, Aug. 22. The BLM simulation is the solid line; measured winds are shown as crosses.

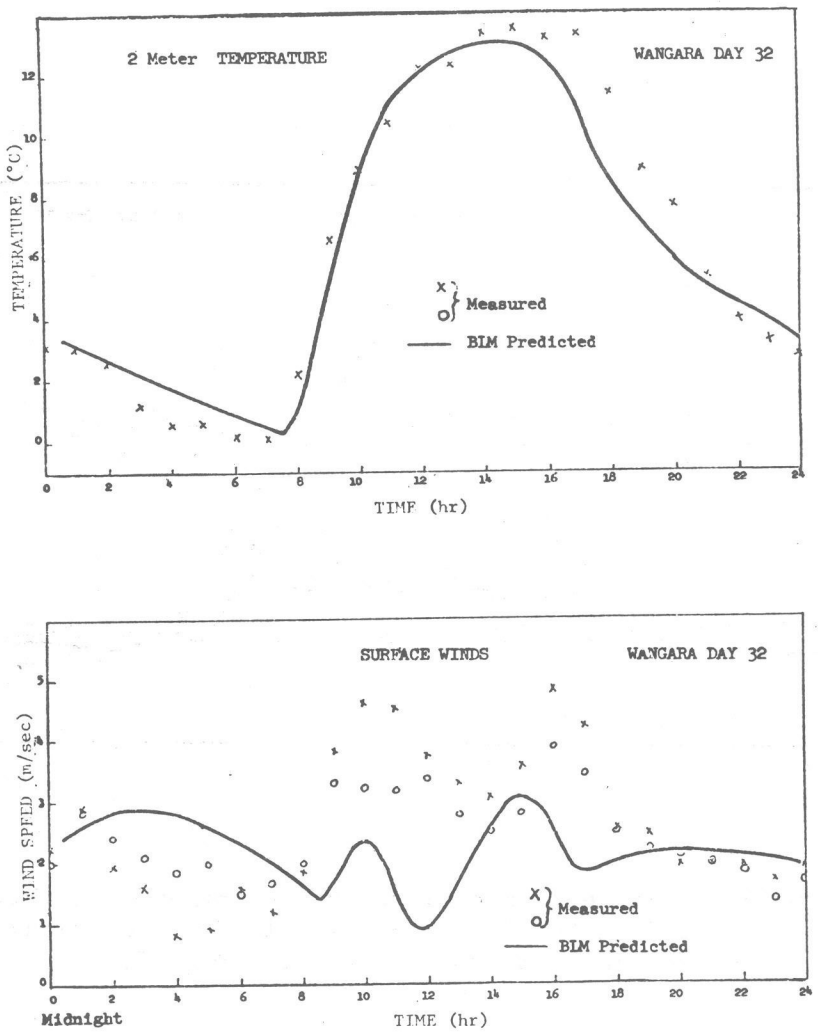

Figure 17.--BLM-simulated surface temperatures and winds are compared with measured values at Wangara, Aug. 15.

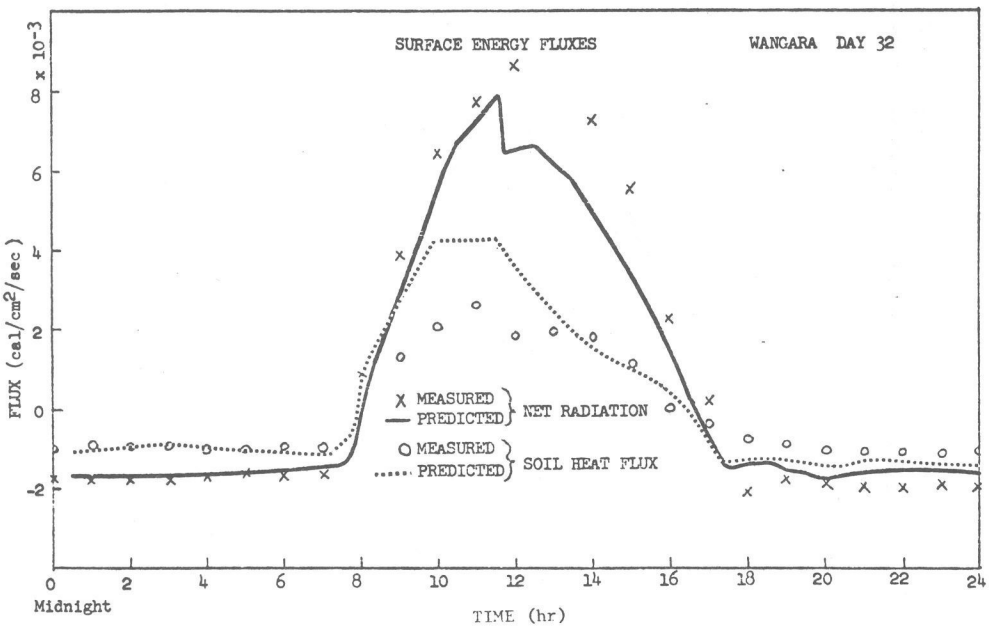

Figure 18.--Surface fluxes of net radiation and soil heat calculated in the BLM simulation are compared to measurements for Wangara, Aug. 15.

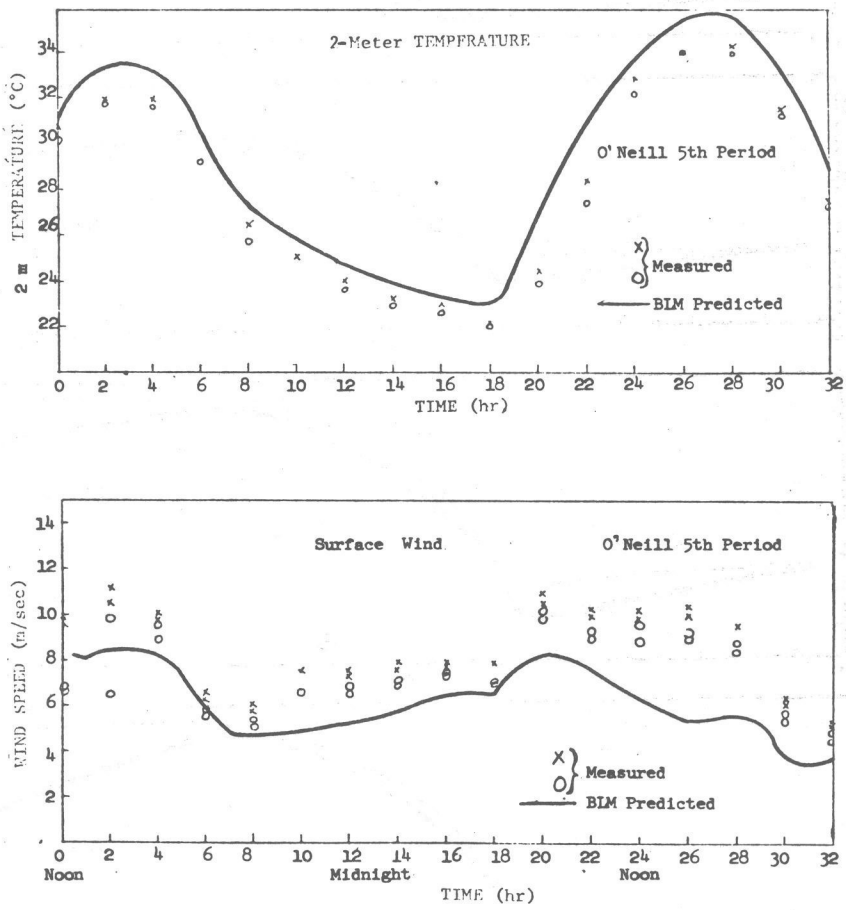

Figure 19.--BLM-simulated surface temperatures and winds are compared with measured values at O'Neill, Nebraska.

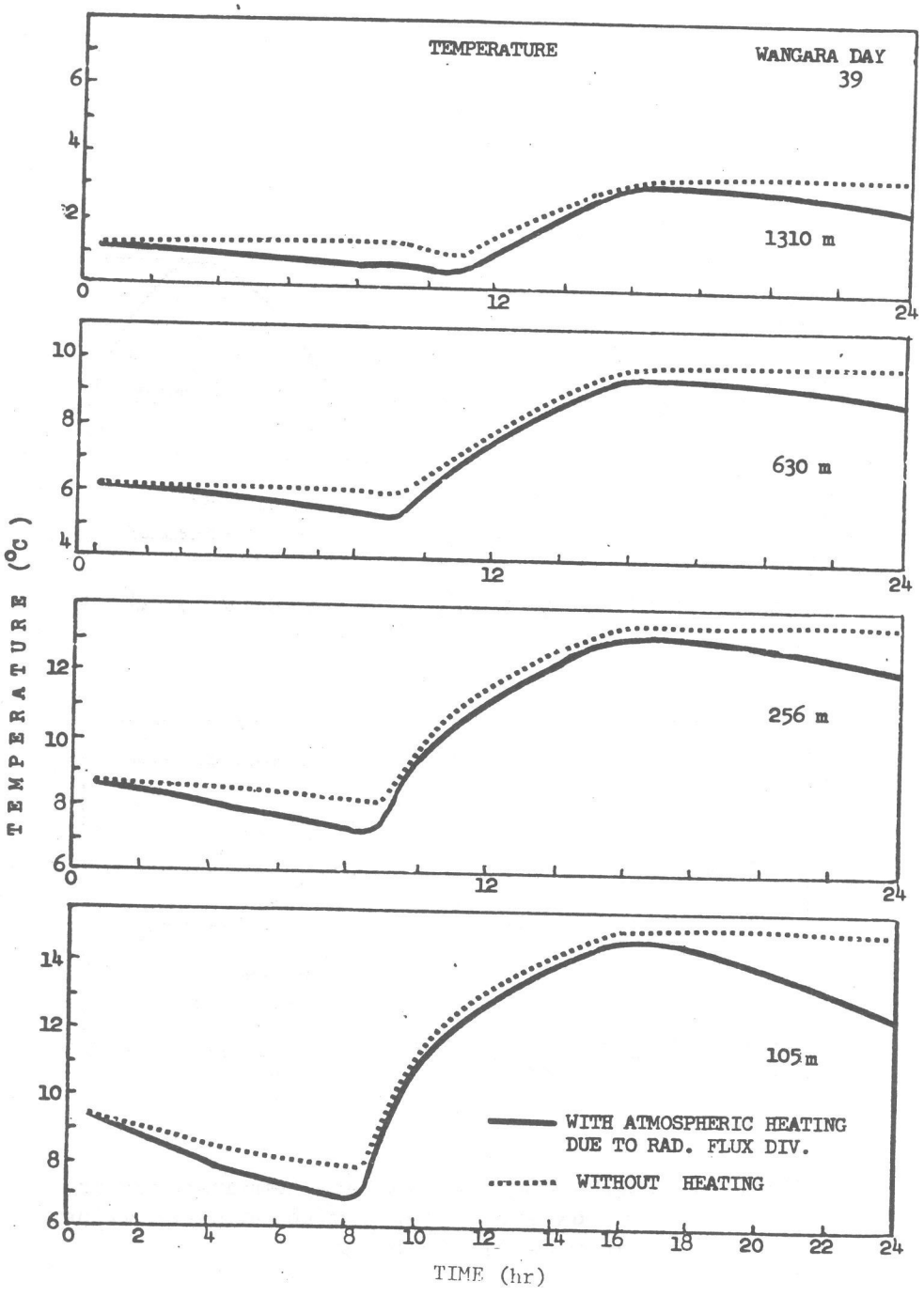

Figure 20.--Results of running the one-dimensional model with and without radiative heating due to flux divergences.

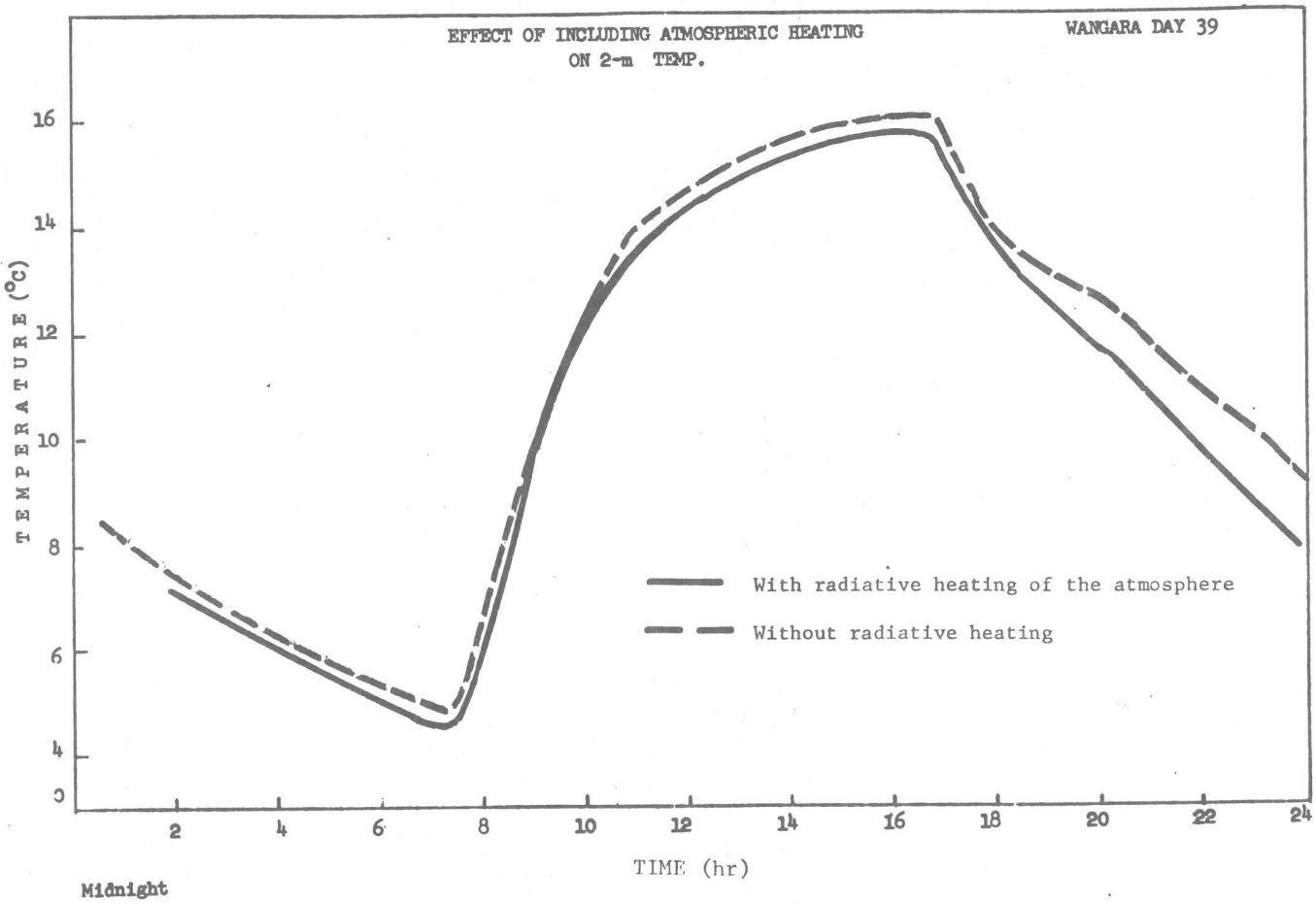

Figure 21.--Surface temperatures are compared for similar runs with and without radiative heating.

Without radiational heating, only during the unstable period of the day are significant temperature changes noted at upper levels. Between 4 PM and 8 AM, temperatures remain virtually constant. As expected, radiative cooling is a major mechanism for nocturnal cooling within the boundary layer. Even the surface temperature is affected (figure 21). Without heating the nocturnal cooling rate is incorrect, leading to an error of roughly 2°C in the minimum temperature for this example.

Interesting experiments were performed by changing the soil characteristics and the initial soil temperature profile for the model. In figure 22, changes in the soil's thermal coefficients most notably affect the nocturnal cooling rate. A 2°C change in the minimum temperature resulted when the model was initialized at midnight. However, the next day's maximum temperature varied by less than 1°C. Undoubtedly, initializing the model at other times will change these values. However, the nocturnal cooling rate will remain the feature most sensitive to thermal coefficient changes.

Figure 23 shows the effects of very large errors in the initial soil temperature profile. The central curve represents a profile in reasonable balance with the atmosphere. The curves bracketing this one result when $\pm$ 5° is added to the initial soil temperature profile. Again, the nocturnal minimum temperature appears to be affected more than the daytime maximum. As the day progresses, the exchange of energy between the atmosphere and soil reduce the surface temperature difference from its initial value of 5° to about 1 1/2°C after 24 hours.

Variations in surface moisture will drastically affect the surface temperature. Depending on the soil moisture available for evaporation and the atmospheric humidity, evaporation can use up from 0% to well over 50% of the net radiation. In figure 24 the humidity factor (E actual/E potential) is varied from 0, a completely dry surface, to 1, corresponding to a saturated surface. Since temperatures are low in this case, the variation is not as drastic as it could be for a warm, dry atmosphere.

IX. SUMMARY AND CONCLUSION

Simulations of several days of real data were carried out using the TDL one-dimensional boundary layer model. Good agreement was obtained between measured and model-predicted winds and temperature near the surface; however, deterioration of predicted values became noticeable as the height was increased. Part of this may be due to not including advective effects.

Both surface temperatures and surface energy fluxes agree well with measurements. The soil heat flux calculation is based on an analytic solution to the heat equation and does not require computation of sub-surface temperature, as does the usual finite-difference treatment. Using this soil heat calculation in the energy balance, changes in the soil's thermal coefficients and the initial soil temperature profile were shown to affect the surface temperature.

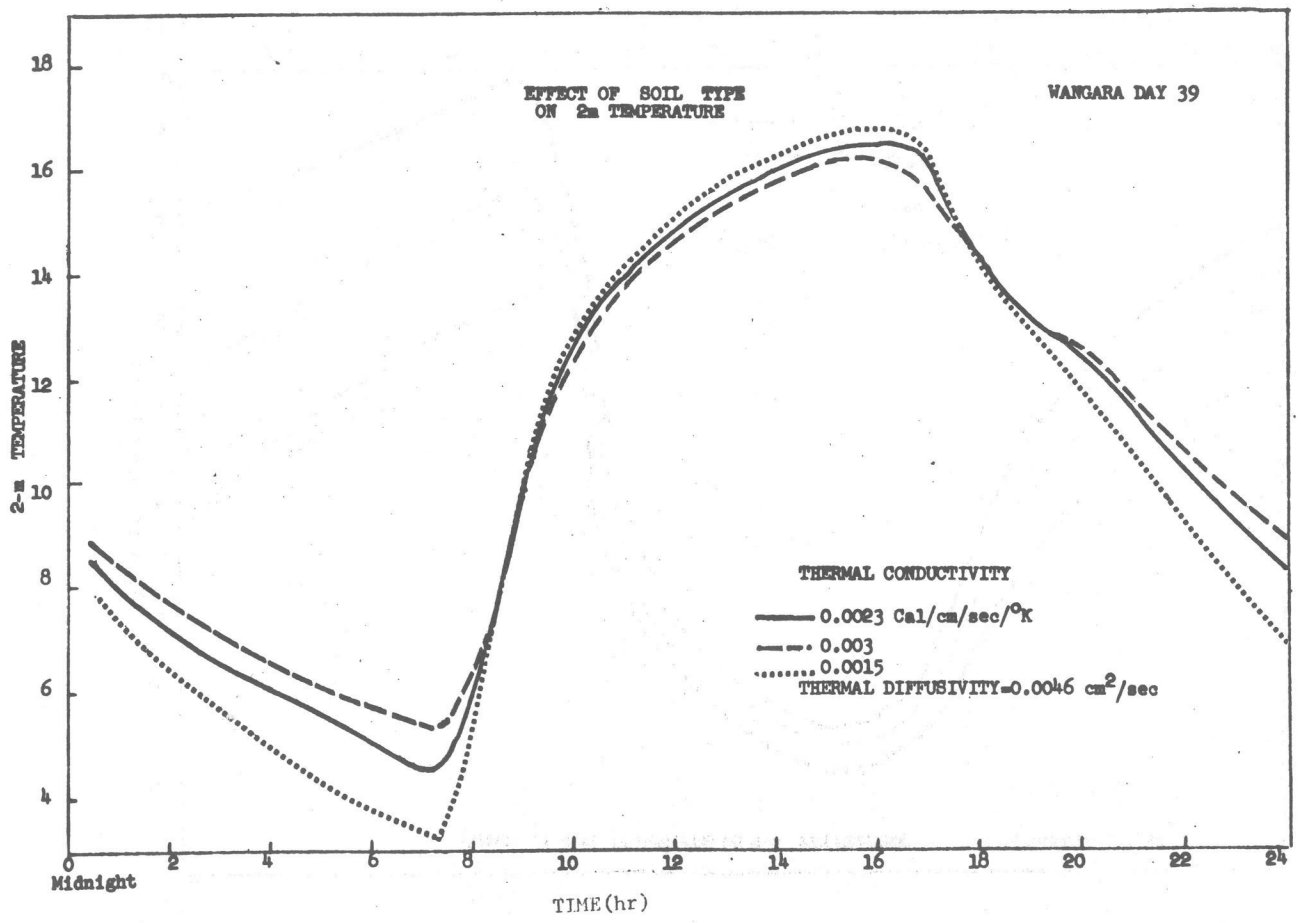

Figure 22.--Changes in surface temperature due to varying the soil's thermal conductivity are shown. The thermal diffusivity was held the same in each case.

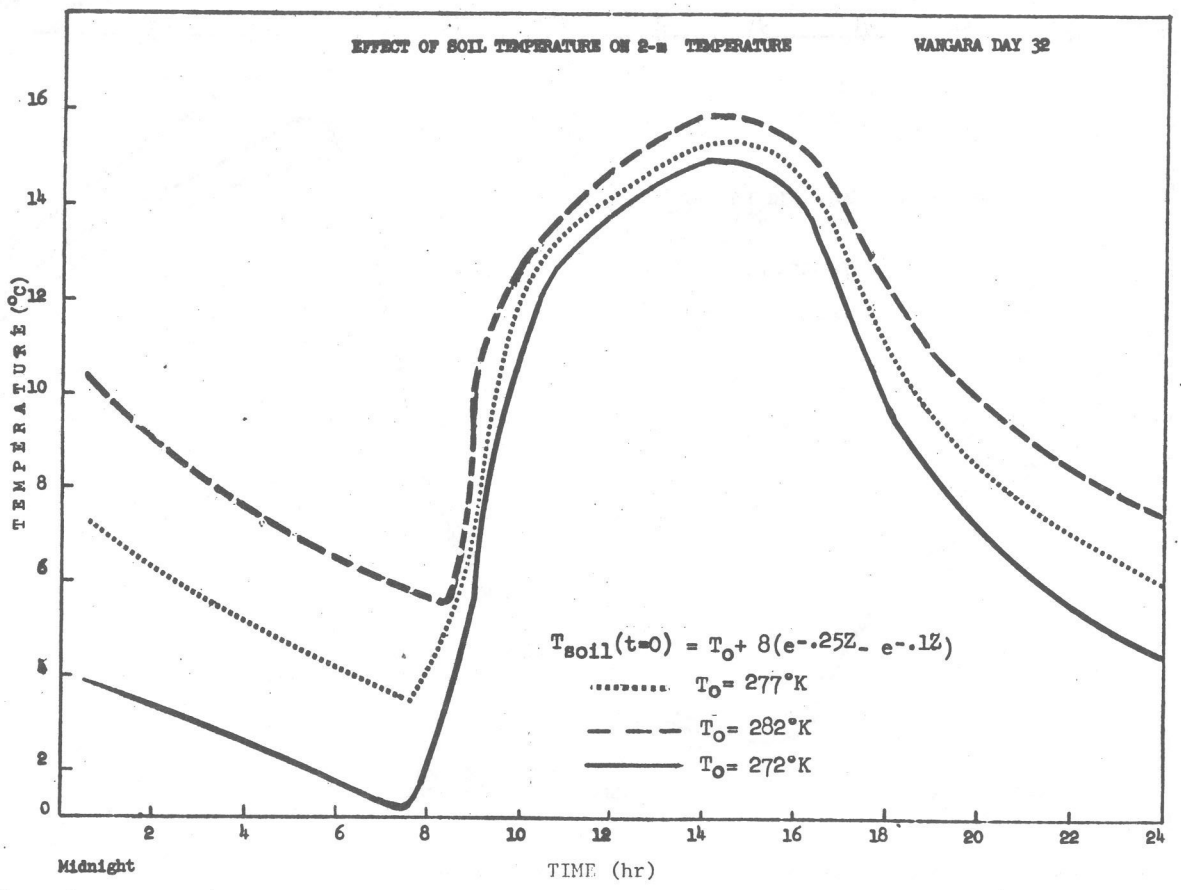

Figure 23.--Surface temperature variation induced by changes in the initial soil temperature.

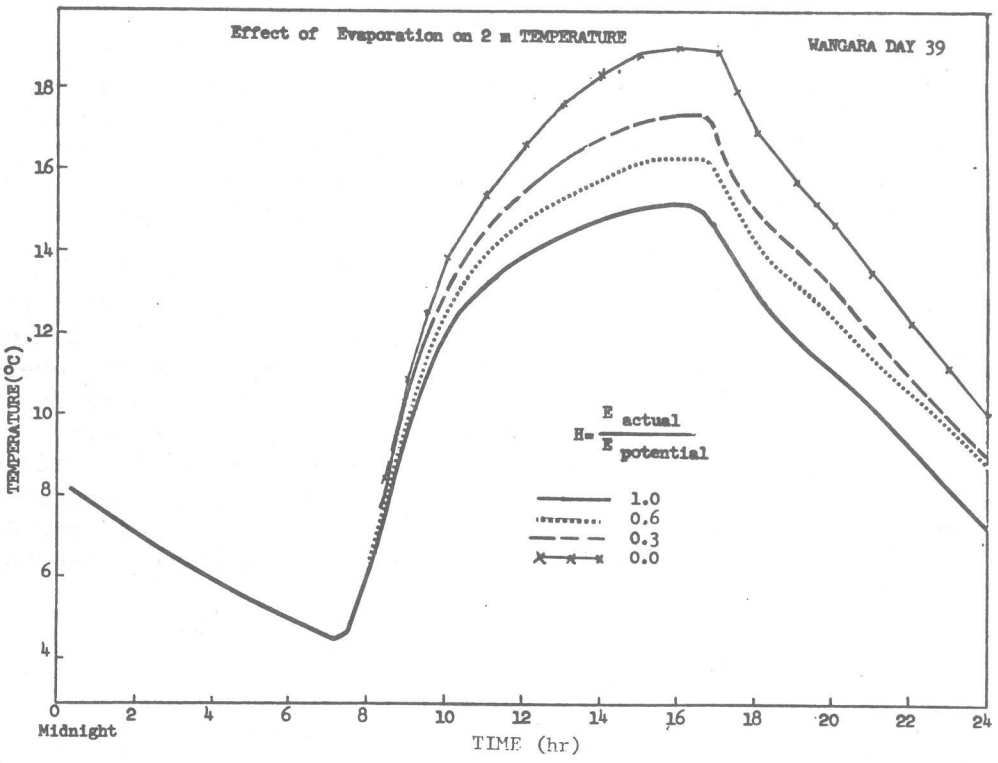

Figure 24.--Surface temperature variation due to changes in the surface moisture specification. H = 1 corresponds to a wet surface; H = 0 is a completely dry surface.

Long wave and solar radiation fluxes and the heating due to their flux divergences are calculated throughout the boundary layer using simple formulations. Heating due to long wave flux divergence was shown to be important in reducing the nocturnal inversion, giving a more realistic diurnal temperature oscillation at intermediate heights.

Efficient, accurate advection and diffusion schemes which allow a long time step have been investigated. We are using a Crank-Nicolson finite-difference scheme for vertical diffusion. For horizontal advection, both the spline and the chapeau function techniques show promise for use in the model; both are efficient and allow a varying grid mesh length to be incorporated easily.

Although the ideas of a constant flux layer and a prescribed diffusion coefficient are inelegant, they are computational expedients. Not using a surface flux layer requires the use of many more computational levels near the surface. The use of shear-dependent diffusion coefficients is being considered but this tends to strain the finite-difference scheme. The use of turbulent energy closure appears far too time consuming for this model. The planned three-dimensional model will operate on a large horizontal grid, 25 grid points on a side. In order to run the model daily, or perhaps twice daily, in the National Weather Service's forecast framework, computer time must be effectively used.

Acknowledgments

The authors wish to thank Miss Farnese Hicks for her assistance in programming and analysis, Mr. Denis Sakelaris for preparing the figures, and both Mrs. Jocelyn Boss and Mrs. Sandra Swab for typing the text.

REFERENCES

Atwater, M. A., 1970: Investigation of the radiation balance for polluted layers of the urban environment. Ph. D. Thesis, New York University, New York, 141 pp.

Businger, J. A., J. C. Wyngaard, Y. Izumi, and E. F. Bradley, 1971: Flux-profile relationships in the atmospheric surface layer. J. Atmos. Sci., 28, 181-189.

Carslaw, H. S., and J. C. Jeager, 1959: Conduction of Heat in Solids. Oxford University Press, London, England, 510 pp.

Clarke, R. H., A. J. Dyer, R. R. Brook. D. G. Reid, and A. J. Troup, 1971: The Wangara Experiment: Boundary Layer Data, Commonwealth Scientific and Industrial Research Organization, Victoria, Australia, 349 pp.

Dyer, A. J., 1967: The turbulent transport of heat and water vapor in an unstable atmosphere. Quart. J. R. Met. Soc., 93, 501-508.

Hadeen, K. D., and A. L. Friend, 1972: The Air Force Global Weather Central operational boundary-layer model. Boundary-Layer Meteorology, 3, 98-112.

Halstead, M. R., R. Richman, W. Covery, and J. Merrman, 1957: A preliminary report on the design of a computer of micrometeorology. J. Meteor., 14, 308-325.

Kondrat'yev, K. Ya., 1969: Radiation in the atmosphere. Int'l. Geophs. Ser., 12, Academic Press, New York, 912 pp.

Kuhn, R. M., 1963: Radiometersonde observations of infrared flux emissivity of water vapor. J. Appl. Meteor., 2, 368-378.

Lettau, H. H., and B. Davidson, 1957: Exploring the Atmosphere's First Mile, Pergamon Press, New York, 578 pp.

Long, P. E., 1975: Dissipation, dispersion and difference schemes. NOAA Technical Memorandum, NWS TDL, No. 56, 33 pp.

Long, P. E., and W. A. Shaffer, 1975: Some physical and numerical aspects of boundary layer modeling. NOAA Technical Memorandum, NWS TDL No. 55, 36 pp.

McDonald, J. E., 1960: Direct absorption of solar radiation by atmospheric water vapor. J. Meteor., 17, 319-328.

O'Brien, J. J., 1970: A note on the veritical structure of the eddy exchange coefficient in the planetary layer. J. Atmos. Sci., 27, 1213-1215.

Pandolfo, J. P., M. A. Atwater, and G. E. Anderson, 1971: Prediction by numerical models of transport and diffusion in an urban boundary layer. The Center for the Environment of Man, Inc., Hartford, Conn.

Webb, E. K., 1970: Profile relationships: The log-linear range, and extension to strong stability. Quart. J. R. Met. Soc., 96, 67-90.

(Continued from inside front cover)

WBTM TDL 25 Charts Giving Station Precipitation in the Plateau States From 850- and 500-Millibar Lows During Winter. August F. Korte, Donald L. Jorgensen, and William H. Klein, September 1969. (PB-187-476)

WBTM TDL 26 Computer Forecasts of Maximum and Minimum Surface Temperatures. William H. Klein, Frank Lewis, and George P. Casely, October 1969. (PB-189-105)

WBTM TDL 27 An Operational Method for Objectively Forecasting Probability of Precipitation. Harry R. Glahn and Dale A. Lowry, October 1969. (PB-188-660)

WBTM TDL 28 Techniques for Forecasting Low Water Occurrences at Baltimore and Norfolk. James M. McClelland, March 1970. (PB-191-744)

WBTM TDL 29 A Method for Predicting Surface Winds. Harry R. Glahn, March 1970. (PB-191-745)

WBTM TDL 30 Summary of Selected Reference Material on the Oceanographic Phenomena of Tides, Storm Surges, Waves, and Breakers. N. Arthur Pore, May 1970. (PB-192-449)

WBTM TDL 31 Persistence of Precipitation at 108 Cities in the Conterminous United States. Donald L. Jorgensen and William H. Klein, May 1970. (PB-193-599)

WBTM TDL 32 Computer-Produced Worded Forecasts. Harry R. Glahn, June 1970. (PB-194-262)

WBTM TDL 33 Calculation of Precipitable Water. L. P. Harrison, June 1970. (PB-193-600)

WBTM TDL 34 An Objective Method for Forecasting Winds Over Lake Erie and Lake Ontario. Celso S. Barrientos, August 1970. (PB-194-586)

WBTM TDL 35 Probabilistic Prediction in Meteorology: a Bibliography. Allan H. Murphy and Roger A. Allen, June 1970. (PB-194-415)

WBTM TDL 36 Current High Altitude Observations--Investigation and Possible Improvement. M. A. Alaka and R. C. Elvander, July 1970. (COM-71-00003)

NOAA Technical Memoranda

NWS TDL-37 Prediction of Surface Dew Point Temperatures. R. C. Elvander, February 1971. (COM-71-00253)

NWS TDL-38 Objectively Computed Surface Diagnostic Fields. Robert J. Bermowitz, February 1971. (COM-71-00301)

NWS TDS-39 Computer Prediction of Precipitation Probability for 108 Cities in the United States. William H. Klein, February 1971. (COM-71-00249)

NWS TDL-40 Wave Climatology for the Great Lakes. N. A. Pore, J. M. McClelland, C. S. Barrientos, and W. E. Kennedy, February 1971. (COM-71-00368)

NWS TDL-41 Twice-Daily Mean Monthly Heights in the Troposphere Over North America and Vicinity. August F. Korte, June 1971. (COM-71-00826)

NWS TDL-42 Some Experiments With a Fine-Mesh 500-Millibar Barotropic Model. Robert J. Bermowitz, August 1971. (COM-71-00958)

NWS TDL-43 Air-Sea Energy Exchange in Lagrangian Temperature and Dew Point Forecasts. Ronald M. Reap, October 1971. (COM-71-01112)

NWS TDL-44 Use of Surface Observations in Boundary-Layer Analysis. H. Michael Mogil and William D. Bonner, March 1972. (COM-72-10641)

NWS TDL-45 The Use of Model Output Statistics (MOS) To Estimate Daily Maximum Temperatures. John R. Annett, Harry R. Glahn, and Dale A. Lowry, March 1972. (COM-72-10753)

NWS TDL-46 SPLASH (Special Program To List Amplitudes of Surges From Hurricanes) I. Landfall Storms. Chester P. Jelesnianski, April 1972. (COM-72-10807)

NWS TDL-47 Mean Diurnal and Monthly Height Changes in the Troposphere Over North America and Vicinity. August F. Korte and DeVer Colson, August 1972. (COM-72-11132)

NWS TDL-48 Synoptic Climatological Studies of Precipitation in the Plateau States From 850-, 700-, and 500-Millibar Lows During Spring. August F. Korte, Donald L. Jorgensen, and William H. Klein, August 1972. (COM-73-10069)

NWS TDL-49 Synoptic Climatological Studies of Precipitation in the Plateau States From 850-Millibar Lows During Fall. August F. Korte and DeVer Colson, August 1972. (COM-74-10464)

NWS TDL-50 Forecasting Extratropical Storm Surges For the Northeast Coast of the United States. N. Arthur Pore, William S. Richardson, and Herman P. Perrotti, January 1974. (COM-74-10719)

NWS TDL-51 Predicting the Conditional Probability of Frozen Precipitation. Harry R. Glahn and Joseph R. Bocchieri, March 1974. (COM-74-10909/AS)

NWS TDL-52 SPLASH (Special Program to List Amplitudes of Surges From Hurricanes) II. General Track and Variant Storm Conditions. Chester P. Jelesnianski, March 1974.

NWS TDL-53 A Comparison Between the Single Station and Generalized Operator Techniques for Automated Prediction of Precipitation Probability. Joseph R. Bocchieri, September 1974. (COM-74-11763/AS)

NWS TDL-54 Climatology of Lake Erie Storm Surges at Buffalo and Toledo. N. Arthur Pore, Herman P. Perrotti, and William S. Richardson, December 1974.

NWS TDL-55 Dissipation, Dispersion and Difference Schemes. Paul E. Long, Jr, in press, 1975.

NWS TDL-56 Some Physical and Numerical Aspects of Boundary Layer Modeling. Paul E. Long, Jr., in press, 1975.